IMPROVED MODELING OF UNSTEADY HEAT TRANSFER
(The First Step)

Mark A. Driver, Ph.D.
Christian Brothers University
650 East Parkway South
Memphis TN 38104

28 February 1995

Final Report for Grant Number F49620-94-1-0292

Approved for public release; distribution unlimited

Prepared for
AIR FORCE OFFICE OF SCIENTIFIC RESEARCH
110 Duncan Avenue
Bolling AFB DC 20332-0001

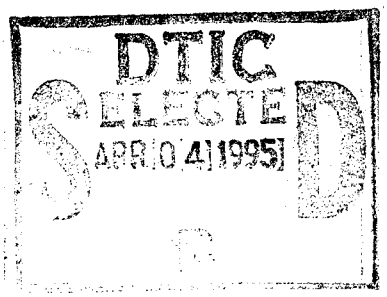

REPORT DOCUMENTATION PAGE

Form Approved
OMB No. 0704-0188

1. AGENCY USE ONLY (Leave blank)	2. REPORT DATE	3. REPORT TYPE AND DATES COVERED
	28 Feb 95	Final 01 Jun 94 - 31 Jul 94

4. TITLE AND SUBTITLE
Improved Modeling of Unsteady Heat Transfer (The First Step)

5. FUNDING NUMBERS
G F49620-94-1-0292

6. AUTHOR(S)
Mark A. Driver, Ph.D.

7. PERFORMING ORGANIZATION NAME(S) AND ADDRESS(ES)
Christian Brothers University
650 East Parkway South
Memphis TN 38104

8. PERFORMING ORGANIZATION REPORT NUMBER
AFOSR-TR-95-0192

9. SPONSORING/MONITORING AGENCY NAME(S) AND ADDRESS(ES)
Air Force Office of Scientific Research
110 Duncan Avenue
Bolling AFB DC 20332-0001

10. SPONSORING/MONITORING AGENCY REPORT NUMBER

11. SUPPLEMENTARY NOTES

12a. DISTRIBUTION/AVAILABILITY STATEMENT
Approved for public release; distribution unlimited

12b. DISTRIBUTION CODE

13. ABSTRACT (Maximum 200 words)

Application of Total Variation Diminishing (TVD) schemes to turbulent flows is considered. The mathematical and physical basis of TVD schemes is discussed.

TVD methodology is extended to the solution of turbulent flow problems. A first-order time accurate, second-order space accurate algorithm is used to compute solutions to the problems of shock-boundary-layer interaction, turbine rotor cascade flow, and unsteady, shock-induced heat transfer using the TVD algorithm. This algorithm provides the capability to accurately predict separation, reattachment and pressure and skin friction profiles for shock-boundary-layer interaction. Improved accuracy is demonstrated in computing surface pressures for a turbine rotor cascade. Heat transfer for the cascade is predicted with fair accuracy, showing all the significant features of the experimental Stanton number profile. Fairly accurate comparison with thery and experiment is evident in the unsteady solutions.

14. SUBJECT TERMS
Numerical Methods and Procedures, Computational Fluid Dynamics, Turbulent Flow, Unsteady Flow, Heat Transfer

15. NUMBER OF PAGES
68

16. PRICE CODE

17. SECURITY CLASSIFICATION OF REPORT	18. SECURITY CLASSIFICATION OF THIS PAGE	19. SECURITY CLASSIFICATION OF ABSTRACT	20. LIMITATION OF ABSTRACT
Unclassified	Unclassfied	Unclassfied	UL

NSN 7540-01-280-5500

Standard Form 298 (Rev. 2-89)
Prescribed by ANSI Std. 239-18
298-102

Acknowledgments

Many people deserve recognition for their contributions to the present effort. I wish to thank Ms. Marilyn McKee, Chief, Contracts/Grants, Administrative Division of AFOSR for her patience and understading during preparation of the final report. I owe a special debt of gratitued to Dr. Daniel Fant, the former Program Manager, for making this effort prossible. I would also like to thank Dr. Philip Beran of the Air Force Institute of Technology and Mr. Robert Boyle of the National Aeronautics and Space Administration for their assistance in providing me with experimental data, blade geometries, and numerous other pieces of critical information. Much is owed to my superiors and colleagues. Many thanks to Dr. Ray Brown, Dean of the School of Engineering, and Dr. Michael Santi, Head of the Mechanical Engineering Department, for their support and enthusiam during this effort. Finally, I never would have been successful in this endeavor without the support of my wife Sheryl, and my sons Lee and Luke. Sheryl unselfishly sacrificed her needs and desires so that I could spend extra time at work, and she was always there to cheer me up when the numbers just weren't working out. Lee and Luke were a constant source of inspiration, and kept me going when a little encouragement was needed.

Mark A. Driver, Ph.D

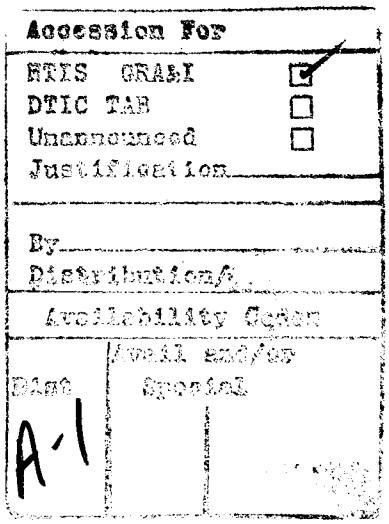

Table of Contents

List of Figures

List of Symbols

Symbol

a - eigenvalue

A - Jacobian matrix

A^+ - Damping coefficient

B - Jacobian matrix

c - speed of sound

C - constant

C_f - skin friction coefficient

Cx - axial chord length

CFL - Courant-Friedrich-Lewy condition

$\bar{D}$ - Roe averaged quantity

e - total energy

f - flux

$\bar{f}$ - numerical flux

F - entropy flux; flux in x direction; function

$\bar{F}$ - numerical entropy flux

$\tilde{F}$ - numerical flux in ξ direction

g - flux limiter

G - flux in y direction

$\tilde{G}$ - numerical flux in η direction

h - convective heat transfer coefficient

H - conservative form; total enthalpy

I - identity matrix

J - Jacobian transformation

k - coefficient of thermal conductivity

k_1 - constant based on metrics

k_2 - constant based on metrics

k_ξ - constant based on metrics

k_η - constant based on metrics

L - operator

$\mathcal{L}$ - Strang fractional step operator

m - x-momentum

msec - millisecond

n - y-momentum

O - order

p - pressure

Pr - Prandtl number

q - dynamic pressure; heat flux

Q - coefficient of numerical viscosity

R - eigenvector

Re - Reynolds number

R_{inv} - Riemann invariant

s - entropy

S - matrix of right eigenvectors

St - Stanton Number

t - time

T - temperature

TV - total variation

u - vector of unknows; x-component of velocity

U - entropy function; vector of dependent variables

v - mesh value; y-component of velocity

V - speed; velocity in non-rotating frame of reference

w - characteristic value

x - distance along the reference x-axis; dummy variable

y - distance along the reference y-axis; normal coordinate

y^+ - boundary layer coordinate

α - difference of characteristic variables

β - numerical dissipation; relative gas angle

δ - central difference operator

Δ - difference

ϵ - entropy correction parameter

λ - time step divided by mesh spacing; second coefficient of viscosity

Λ - diagonal matrix of eigenvalues

μ - first coefficient of viscosity; CFL (Courant) number

θ - Beam-Warming time discretization parameter

ϕ - initial condition

Φ - artificial dissipation vector

ψ - entropy correction; viscous derivative term

Ψ - numerical viscous derivative function

ξ, η - transformed coordinates

γ - ratio of specific heats

ρ - density

τ - shear stress

ω - Beam-Warming damping coefficient

Subscripts

aw - adiabatic wall

cr - condition at a Mach number of unity

e - explicit

i - implicit

int - quantity extrapolated from domain interior

j - ξ index

k - η index

L - left

n - normal; normal derivative

R - right; relative to rotating reference frame

s - shock conditions

t - differentiation w.r.t t; stagnation condition; tangential; turbulent

u - differentiation w.r.t u

v - viscous; differentiation w.r.t v

w - evaluated at wall

x - differentiation w.r.t x

y - differentiation w.r.t y

η - η direction; differentiation w.r.t η

ξ - ξ direction; differentiation w.r.t ξ

∞ - condition at upstream infinity

1 - condition at stator exit

2 - condition at rotor inlet

3 - condition at rotor exit

Superscripts

h - time step

l - vector component

n - time level

η - η direction

ξ - ξ direction

$\wedge$ - strong conservation form

Abstract

Application of Total Variation Diminishing (TVD) schemes to turbulent flows is considered. The mathematical and physical basis of TVD schemes is discussed.

TVD methodology is extended to the solution of turbulent flow problems. A first-order time accurate, second-order space accurate algorithm is used to compute solutions to the problems of shock-boundary-layer interaction, turbine rotor cascade flow, and unsteady, shock-induced heat transfer using the TVD algorithm. This algorithm provides the capability to accurately predict separation, reattachment, and pressure and skin friction profiles for shock-boundary-layer interaction. Improved accuracy is demonstrated in computing surface pressures for a turbine rotor cascade. Heat transfer for the cascade is predicted with fair accuracy, showing all the significant features of the experimental Stanton number profile. Fairly accurate comparison with theory and experiment is evident for the unsteady, shock-induced heat transfer problem, with the exception being failure to correctly predict transition for this case.

IMPROVED MODELING OF UNSTEADY HEAT TRANSFER
(The First Step)

I. Mathematical and Physical Basis of TVD Schemes

1.1 The Genesis of TVD

Total Variation Diminishing (TVD) schemes, originally refered to as Total Variation Nonincreasing (TVNI), first appeared in 1983 with the publication of Harten's *High Resolution Schemes for Hyperbolic Conservation Laws* [23]. In general, TVD schemes are arrived at by applying a first-order accurate numerical method to an appropriately modified flux function thus yielding a method that is second-order accurate except near points of extrema of the solution. The genesis of the TVD class of finite-difference schemes can be traced to 1976 when Harten, Hyman, and Lax authored *On Finite-Difference Approximations and Entropy Conditions for Shocks* [24]. This work first addressed the question of whether finite-difference approximations to the solution of hyperbolic conservation laws converge to the physically relevant solution. This is of interest because weak solutions to such conservation laws are not uniquely determined by initial values, but require an entropy condition be met to converge to the particular physical solution [24].

In the mid 1970's, Harten was also working on his artificial compression method (ACM) [20] to modify standard finite-difference schemes in an effort to prevent the smearing of contact surfaces and improve shock resolution [21, 22]. Prior to this effort, Harten states that the standard finite-difference schemes in use typically smeared shocks over 3–5 cells while the width of the contact surface behaved as $n^{1/(R+1)}$ where n is the total number of time steps taken and R is the scheme's order of accuracy. Harten's ACM also addressed the fact that schemes of order greater

than one produced overshoots and undershoots around the discontinuity [21] and forced the approximated solution to be nonphysical [24]. Harten's ACM modifications to existing schemes provided the foundation for the new class of TVD schemes presented in his 1983 paper.

The rigorous mathematical foundation of TVD schemes is mainly confined to scalar linear and nonlinear conservation laws and is painstakingly outlined in references [24] and [23]. Computational fluid dynamicists are interested in applying TVD schemes to systems of nonlinear hyperbolic conservation laws, such as the Euler equations of gasdynamics. Therefore, Harten details the application of TVD methodology to 1-D systems using Roe's approximate Riemann solver and provides an example of its extension to 2-D using Strang's dimensional splitting [23]. The original Harten scheme was a second-order accurate explicit method but was extended to a second-order accurate implicit method by Yee and Harten [40].

The high-resolution TVD approach soon gathered favor; explicit and implicit variations were then applied to the Euler equations in general geometries by Yee and Kutler [41] and by Yee and Harten [43]. Later, Wang and Widhopf further extended Harten's TVD methodology to a finite-volume scheme for the Euler equations [44]. TVD algorithms have continued to develop over the past decade. Harten's original scheme was of the upwind variety, meaning that the modifications to the flux function are applied based on the direction of wave propagation, or characteristic direction. Symmetric algorithms have since come into use where the modifications are applied without regard to the characteristic directions. Methods are also available for partial differential equations with source terms and stiff source terms. Yee's 1989 publication,*A Class of High-Resolution Explicit and Implicit Shock-Capturing Methods* [42], provides detailed information on numerous versions of TVD algorithms and examples of their application to numerous problems.

1.2 *Hyperbolic Conservation Laws and TVD Methodology*

The present section provides a description of the hyperbolic conservation laws for which TVD schemes provide solutions. The requirements for uniqueness of a solution to the initial value problem are given along with the necessary conditions to guarantee convergence of a finite difference approximation to this solution. A summary is provided of the methodology behind the construction of Harten's original second-order accurate TVD scheme.

1.2.1 Finite-Difference Schemes and Oleinik's Entropy Condition. The present analysis is concerned with weak solutions of the initial value problem

$$\begin{aligned} & u_t + f(u)_x = 0 \\ & \qquad\qquad -\infty < x < \infty \\ & u(x,0) = \phi(x) \end{aligned} \tag{1.1}$$

where $u(x,t)$ is a column vector of m unknowns, $f(u)$ is the flux vector of m components, and $\phi(x)$ is the initial data. Eq 1.1 is hyperbolic if all eigenvalues $a^1(u), \ldots, a^m(u)$ of the Jacobian matrix

$$A(u) = f_u \tag{1.2}$$

are real and the set of right eigenvectors $R^1(u), \ldots, R^m(u)$ is complete [23] over the domain.

Following Harten [23], consider systems of conservation laws, Eq 1.1, possessing an entropy function $U(u)$ defined such that

$$\begin{aligned} U_{uu} &> 0 \\ U_u f_u &= F_u \end{aligned} \tag{1.3}$$

where F is a function known as the entropy flux [23].

The class of all weak solutions to Eq 1.1 is too large in that the initial value problem is not unique [24]. An additional constraining relation is needed if the scheme is to choose the physically relevant solution. This additional constraint is known as Oleinik's entropy condition and can be expressed as [24]

$$U(u)_t + F(u)_x \leq 0 \tag{1.4}$$

Let us now consider numerical solutions to Eq 1.1 obtained using a $(2k+1)$ point explicit scheme in conservation form [24]. A scheme is in conservation form if it can be expressed as

$$v_j^{n+1} = v_j^n - \lambda \left(\bar{f}_{j+1/2}^n - \bar{f}_{j-1/2}^n \right) \tag{1.5}$$

where

$$\bar{f}_{j+1/2}^n = \bar{f} \left(v_{j-k+1}^n, \ldots, v_{j+k}^n \right) \tag{1.6}$$

and $\lambda = \Delta t / \Delta x$. In Eqs 1.5 and 1.6, $\bar{f}$ is the "numerical" , or mesh, flux function consistent with $f(u)$ in that $\bar{f}(u, \ldots, u) = f(u)$. The solution u is approximated on the mesh by $v_j^n = v(j\Delta x, n\Delta t)$. The numerical scheme given by Eq 1.5 is consistent with the entropy condition, Eq 1.4, if

$$U_j^{n+1} \leq U_j^n - \lambda \left(\bar{F}_{j+1/2}^n - \bar{F}_{j-1/2}^n \right) \tag{1.7}$$

where $U_j^n = U\left(v_j^n\right)$, $\bar{F}_{j+1/2}^n = \bar{F}\left(v_{j-k+1}^n, \ldots, v_{j+k}^n\right)$, and $\bar{F}$ is the numerical entropy flux consistent with $F(u)$ such that $\bar{F}(u, \ldots, u) = F(u)$

The question of convergence of the finite difference scheme, Eq 1.5, to the appropriate weak solution of Eq 1.1 must now be addressed. The scheme under consideration is nonlinear, so stability of a consistent scheme does not imply convergence. Harten [23] outlines three conditions which, when satisfied, ensure convergence.

(1) The total variation (TV) of the finite difference scheme is uniformly bounded, where

$$TV(v) = \sum_{j=-\infty}^{\infty} |v_{j+1} - v_j| \tag{1.8}$$

(2) The scheme is consistent, as $\Delta x \to 0$, with Oleinik's entropy condition for all entropy functions of Eq 1.1.

(3) Oleinik's entropy condition implies a unique solution of the initial value problem for Eq 1.1.

The reader is referred to the references given by Harten [23] for the arguments that imply convergence given satisfaction of the above criteria. For the present work, the validity of these criteria will be assumed and the effort concentrated on demonstrating the development of a scheme that satisfies criteria (1) and (2) when given the third criterion.

1.2.2 Development of Harten's Second-Order Scalar TVD Scheme. Harten's second-order accurate TVD scheme is the product of a nonoscillatory, first-order accurate scheme applied to an appropriately modified flux function [23]. This section describes the properties of the first-order scheme and outlines the procedure used by Harten to arrive at the appropriate modified flux.

Consider the initial value problem for a scalar conservation law:

$$\begin{aligned} & u_t + f(u)_x \equiv u_t + a(u)u_x = 0 \\ & a(u) = f_u \qquad\qquad -\infty < x < \infty \\ & u(x,0) = \phi(x) \end{aligned} \tag{1.9}$$

where $\phi(x)$ is of bounded total variation. Rigorous analysis is restricted to the scalar case because TVD schemes are not defined for systems of of non-linear conservation

laws where the spatial total variation of the solution may increase due to wave interaction [23].

A weak solution of Eq 1.9 has a monotonicity property [23], as a function of time, defined as:

(1) No new local extrema in x may be created.

(2) A local minimum is nondecreasing and a local maximum is nonincreasing.

The monotonicity property implies that the total variation in x is nonincreasing in time, $TV\left(u\left(t_2\right)\right) \leq TV\left(u\left(t_1\right)\right)$.

An explicit, $(2k+1)$, point finite-difference scheme in conservation form, as given by Eq 1.5 and applied to Eq 1.9, can be written as

$$\begin{aligned} v_j^{n+1} &= H\left(v_{j-k}^n, \ldots, v_{j+k}^n\right) \\ &= v_j^n - \lambda\left[\bar{f}\left(v_{j-k+1}^n, \ldots, v_{j+k}^n\right) - \bar{f}\left(v_{j-k}^n, \ldots, v_{j+k-1}^n\right)\right] \end{aligned} \tag{1.10}$$

or in operator notation as

$$v^{n+1} = L \cdot v^n \tag{1.11}$$

The scheme given by Eq 1.10 is TVD if, for all v of bounded total variation

$$TV(L \cdot v) \leq TV(v) \tag{1.12}$$

where the total variation is defined by Eq 1.8. Eq 1.11 represents a monotonicity preserving scheme if the operator L is monotonicity preserving. That is, if v is a monotonic mesh function so is $L \cdot v$. The scheme is monotone if H is a monotonic nondecreasing function of each of its $2k+1$ arguments [24]:

$$H_{w_i}\left(w_{-k}, \ldots, w_k\right) \geq 0 \tag{1.13}$$

for all i such that $-k \leq i \leq k$.

An example of a scheme that is not monotone is the second-order accurate Lax-Wendroff scheme with

$$\bar{f}_{j+\frac{1}{2}} = \frac{1}{2}\left[f\left(v_j^n\right) + f\left(u_{j+1}^n\right) - a^2\lambda\Delta_{j+\frac{1}{2}}v^n\right] \tag{1.14}$$

where $\Delta_{j+\frac{1}{2}}v = v_{j+1} - v_j$. Therefore the discrete equation is

$$\begin{aligned} v_j^{n+1} &= v_j^n - \tfrac{1}{2}\lambda\left[f\left(v_{j+1}^n\right) - f\left(v_{j-1}^n\right) - a^2\lambda\left(v_{j+1}^n - 2v_j^n + v_{j-1}^n\right)\right] \\ &= H\left(v_{j-1}^n, v_j^n, v_{j+1}^n\right) \end{aligned} \tag{1.15}$$

Taking the derivative of H with respect to the argument v_{j+1}^n yields

$$H_{v_{j+1}} = \frac{1}{2}\left(\nu^2 - \nu\right) \tag{1.16}$$

where $\nu = a\lambda$. Only the case $0 < \nu < 1$ need be examined since the Law-Wendroff scheme is unstable for $\nu > 1$, and Lax-Wendroff provides the exact solution for $\nu = 1$. Clearly, the Lax-Wendroff scheme is not monotone for any $\nu < 1$. Additionally, the numerical results of reference [24] show that the Lax-Wendroff scheme is not monotonicity preserving.

The first-order accurate Roe scheme provides an example of monotone behavior. The numerical flux for the Roe scheme is

$$\bar{f}_{j+\frac{1}{2}} = \frac{1}{2}\left[f\left(v_j^n\right) + f\left(u_{j+1}^n\right) - |a|\Delta_{j+\frac{1}{2}}v^n\right] \tag{1.17}$$

giving the discrete equation

$$\begin{aligned} v_j^{n+1} &= v_j^n - \tfrac{1}{2}\lambda\left[f\left(v_{j+1}^n\right) - f\left(v_{j-1}^n\right) - |a|\left(v_{j+1}^n - 2v_j^n + v_{j-1}^n\right)\right] \\ &= H\left(v_{j-1}^n, v_j^n, v_{j+1}^n\right) \end{aligned} \tag{1.18}$$

Taking derivatives of H with respect to each of its arguments gives

$$\begin{aligned} H_{v_{j-1}} &= \nu \\ H_{v_j} &= 1-\nu \\ H_{v_{j+1}} &= 0 \end{aligned} \tag{1.19}$$

Thus, H is a monotonic, non-decreasing function of each of its arguments showing that the Roe scheme is indeed monotonic.

Let S_M, S_{TVD}, and S_{MP} denote monotone, TVD, and monotonicity preserving schemes respectively. Theorem 2.1 of reference [23] provides the hierarchy of these properties:

$$S_M \subset S_{TVD} \subset S_{MP} \tag{1.20}$$

Thus, the Roe scheme is also TVD and monotonicity preserving.

A scheme in the conservation form of Eq 1.10 that is monotone with v_j^n converging boundedly almost everywhere to some function $u(x,t)$ has two further desirable properties. The theorem of Lax and Wendroff as given by reference [24] states that if the scheme is in conservation form with $v(x,t)$ converging almost everwhere to $u(x,t)$, then $u(x,t)$ is a weak solution of Eq 1.9. The theorem of Harten, Hyman, and Lax [24] states that if the scheme is monotone in addition to meeting the criteria of the Lax-Wendroff theorem, then Oleinik's entropy condition is satisfied for all discontinuities of u. Thus a monotone scheme satisfies the convergence criteria for a unique solution of the initial value problem as stated in the Section 1.2.1.

Attention is now focused on how the properties of a monotone scheme are helpful in constructing Harten's second-order TVD scheme. Harten states that monotone schemes provide second-order accurate solutions to the modified Eq [23]

$$u_t + f(u)_x = \Delta t \left[\beta(u,\lambda) u_x\right]_x \tag{1.21}$$

$$\beta(u,\lambda) = \frac{1}{2\lambda^2}\left[\sum_{l=-k}^{k} l^2 H_l(u,\ldots,u) - \lambda^2 a^2(u)\right] \tag{1.22}$$

$$\beta(u,\lambda) \geq 0$$

$$\beta(u,\lambda) \neq 0$$

where β is a numerical dissipation term. Since $\beta(u,\lambda) \neq 0$, monotone schemes are only first-order accurate approximations to the initial value problem of Eq 1.9.

Suppose the scheme given by Eq 1.10 is a monotone scheme and thus provides a second-order accurate numerical approximation to the modified equation, Eq 1.21, rewritten as

$$u_t + (f - (1/\lambda)g)_x = 0 \tag{1.23}$$

where $g = \Delta x \beta(u,\lambda) u_x$. Applying this scheme to the following equation

$$u_t + (f + (1/\lambda)g)_x = 0 \tag{1.24}$$

yields a second-order accurate approximation to its modified equation. Since $g = O[\Delta x]$ the modified equation satisfies [23]

$$u_t + f_x = O\left[(\Delta x)^2\right] \tag{1.25}$$

Thus, application of a first-order scheme to a scalar conservation law with an appropriately modified flux function yields a second-order accurate approximation to the original equation $u_t + f_x = 0$. Note that in order to apply the scheme to the modified flux function, g must be a differentiable function of u. Harten achieves this by smoothing the point values of g [23]. This smoothing enlarges the support of the scheme such that his first-order scheme, using a three-point stencil, becomes a second-order scheme using a five-point stencil. The reader is referred to reference [23] for the details of how the three-point, first-order scheme is constructed so as to ensure

its TVD property.

Let us now turn our attention to the specific scalar scheme developed by Harten. Consider a three-point, finite-difference scheme in conservation form with the following numerical flux function

$$\bar{f}\left(v_j, v_{j+1}\right) = \frac{1}{2}\left[f\left(v_j\right) + f\left(v_{j+1}\right) - (1/\lambda)Q\left(\lambda \bar{a}_{j+1/2}\right)\Delta_{j+1/2}v\right] \tag{1.26}$$

where $\Delta_{j+1/2}v = v_{j+1} - v_j$ and

$$\begin{aligned} \bar{a} &= \left[f\left(v_{j+1}\right) - f\left(v_j\right)\right]/\Delta_{j+1/2}v \quad \left(\Delta_{j+1/2}v \neq 0\right) \\ &= a\left(v_j\right) \qquad\qquad\qquad\qquad\quad \left(\Delta_{j+1/2}v = 0\right) \end{aligned} \tag{1.27}$$

Q is a function known as the coefficient of numerical viscosity. Numerical viscosity is the mechanism that allows a discontinuity to be captured as part of the numerical solution [21]. This is in contrast to shock fitting, where the discontinuity is considered as an internal boundary.

Lemma 3.1 of reference [23] states that the above scheme is TVD under the Courant-Friedrichs-Lewy (CFL) condition

$$\lambda \max_j \left|\bar{a}^n_{j+1/2}\right| \leq \mu \tag{1.28}$$

given

$$|x| \leq Q(x) \leq 1 \tag{1.29}$$

for $0 \leq |x| \leq \mu \leq 1$.

The first-order accurate three-point scheme given by Eq 1.26 is converted to a second-order accurate scheme by applying the three-point scheme to modified flux

values f_j^M [23]:

$$\begin{aligned} f_j^M &= f(v_j) + (1/\lambda) g_j & g_j &= g(v_{j-1}, v_j, v_{j+1}) \\ \bar{\nu}_{j+1/2}^M &= \bar{\nu}_{j+1/2} + \gamma_{j+1/2} & \gamma_{j+1/2} &= (g_{j+1} - g_j) / \Delta_{j+1/2} v \end{aligned} \tag{1.30}$$

where $\bar{\nu} \equiv \lambda \bar{a}$. The modified numerical flux is

$$\begin{aligned} \bar{f}_{j+1/2}^M &= \tfrac{1}{2}\left[f_j^M + f_{j+1}^M - (1/\lambda) Q\left(\bar{\nu}_{j+1/2}^M\right) \Delta_{j+1/2} v\right] \\ &= \tfrac{1}{2}\left[f(v_j) + f(v_{j+1})\right] \\ &\quad + (1/(2\lambda))\left[g_j + g_{j+1} - Q\left(\bar{\nu}_{j+1/2} + \gamma_{j+1/2}\right) \Delta_{j+1/2} v\right] \end{aligned} \tag{1.31}$$

Lemma 3.2 of reference [23] provides that Eq 1.31 represents the numerical flux of a second-order scheme so long as $Q(x)$ is Lipschitz continuous and g_j satisfies

$$\begin{aligned} g_j + g_{j+1} &= \left[Q\left(\bar{\nu}_{j+1/2}\right) - \left(\bar{\nu}_{j+1/2}\right)^2\right] \Delta_{j+1/2} v + O[2] \\ \gamma_{j+1/2} \Delta_{j+1/2} v &\equiv g_{j+1} - g_j = O(\Delta^2) \end{aligned} \tag{1.32}$$

Harten [23] constructs g in the following manner so as to satisfy Eq 1.32:

$$\begin{aligned} g_j &= s_{j+1/2} \max\left[0, \min\left(\left|\tilde{g}_{j+1/2}\right|, \tilde{g}_{j-1/2} \cdot s_{j+1/2}\right)\right] \\ &= s_{j+1/2} \min\left(\left|\tilde{g}_{j+1/2}\right|, \left|\tilde{g}_{j-1/2}\right|\right) && \left(\tilde{g}_{j+1/2} \cdot \tilde{g}_{j-1/2} \geq 0\right) \\ &= 0 && \left(\tilde{g}_{j+1/2} \cdot \tilde{g}_{j-1/2} \leq 0\right) \end{aligned} \tag{1.33}$$

where

$$\begin{aligned} \tilde{g}_{j+1/2} &= \tfrac{1}{2}\left[Q\left(\bar{\nu}_{j+1/2}\right) - \left(\bar{\nu}_{j+1/2}\right)^2\right] \Delta_{j+1/2} v \\ s_{j+1/2} &= sgn\left(\tilde{g}_{j+1/2}\right) \end{aligned} \tag{1.34}$$

Finally, Lemma 3.4 of reference [23] provides that a conservative finite difference scheme, with the numerical flux given by Eq 1.26, is TVD under the restriction of Eq 1.28 so long as $Q(x)$ satisfies Eq 1.29. Thus a second-order accurate (except near points of extrema where $s_{j+1/2}$ is discontinous), five-point scheme has been con-

structed for the solution of Eq 1.9. The scheme provides high resolution capturing of discontinuities and converges to a physically relevant solution.

1.2.3 Extension to Systems of Conservation Laws. We now concern ourselves with extending the scalar scheme developed in Section 1.2.2 to systems of conservation laws. Currently, TVD schemes are only defined for scalar hyperbolic conservation laws or constant coefficient hyperbolic systems. This is due to the fact that the spatial total variation of the solution to a system of nonlinear conservation laws is not necessarily a monotonically decreasing function of time [43]. Wave interactions may cause the total variation to increase. Harten extends the technique using a generalized version of Roe's approximate Riemann solver [23]. The idea is to apply the scheme in a scalar fashion to each of the systems linearized characteristic variables.

After Harten [23], let

$$S(u) = \left(R^1(u), \ldots, R^m(u)\right) \tag{1.35}$$

be a matrix whose columns are the right eigenvectors of the Jacobian matrix $A(u)$ in Eq 1.1. It follows that

$$S^{-1}AS = \Lambda \tag{1.36}$$

where Λ is the diagonal matrix of eigenvalues such that $\Lambda_{ij} = a^i(u)\delta_{ij}$. Therefore

$$S^{-1}u_t + S^{-1}A(u)SS^{-1}u_x = 0 \tag{1.37}$$

or

$$S^{-1}u_t + \Lambda S^{-1}u_x = 0 \tag{1.38}$$

where the characteristic variables w are defined such that

$$w = S^{-1}u \tag{1.39}$$

Eq 1.38 becomes

$$w_t + \Lambda w_x = 0 \tag{1.40}$$

which can be decoupled into m scalar characteristic equations with $1 \leq k \leq m$

$$w_t^k + a^k w_x^k = 0 \tag{1.41}$$

The most beneficial use of the characteristic variables comes to light by recognizing that they can be viewed as the components of u in the coordinate system $\{R^k\}$ such that [23]

$$u = \sum_{k=1}^{m} w^k R^k \tag{1.42}$$

Harten uses this fact to extend his scalar scheme to general nonlinear systems of hyperbolic conservation laws.

Let $\alpha_{j+1/2}^k$ be the component of $\Delta_{j+1/2} v = v_{j+1} - v_j$ in the $\{R^k\}$ coordinate system such that

$$\Delta_{j+1/2} v = \sum_{k=1}^{m} \alpha_{j+1/2}^k R_{j+1/2}^k \tag{1.43}$$

The scheme given by Eqs 1.30–1.34 is extended to general systems as

$$v_j^{n+1} = v_j^n - \lambda \left(\bar{f}_{j+1/2}^n - \bar{f}_{j-1/2}^n \right) \tag{1.44}$$

$$\begin{aligned} \bar{f}_{j+1/2} &= \tfrac{1}{2} \left[f\left(v_j\right) + f\left(v_{j+1}\right) \right] \\ &\quad + \tfrac{1}{2\lambda} \textstyle\sum_{k=1}^{m} R_{j+1/2}^k \left[g_j^k + g_{j+1}^k - Q^k \left(\bar{\nu}_{j+1/2}^k + \gamma_{j+1/2}^k \right) \alpha_{j+1/2}^k \right] \end{aligned} \tag{1.45}$$

where $\nu_{j+1/2}^k = \lambda a_{j+1/2}^k$ and

$$g_j^k = s_{j+1/2}^k \max \left[0, \min \left(\left| \tilde{g}_{j+1/2}^k \right|, \tilde{g}_{j-1/2}^k \cdot s_{j+1/2}^k \right) \right] \tag{1.46}$$

with

$$\begin{aligned} \tilde{g}^k_{j+1/2} &= \tfrac{1}{2}\left[Q^k\left(\tilde{\nu}^k_{j+1/2}\right) - \left(\tilde{\nu}^k_{j+1/2}\right)^2\right]\alpha^k_{j+1/2} \\ s^k_{j+1/2} &= sgn\left(\tilde{g}^k_{j+1/2}\right) \\ \gamma^k_{j+1/2} &= \left(g^k_{j+1} - g^k_j\right)/\alpha^k_{j+1/2} \qquad \left(\alpha^k_{j+1/2} \neq 0\right) \\ &= 0 \qquad \left(\alpha^k_{j+1/2} = 0\right) \end{aligned} \tag{1.47}$$

1.2.4 Entropy Enforcement. As a final comment on the initial development of Harten's second-order TVD scheme, we turn now to the question of physically relevant solutions for systems of equations. As mentioned in the previous section, the total variation may not be a monotonic decreasing function of time due to wave interactions. In addition, Oleinik's entropy inequality ensures physically relevant, or admissable, solutions only in the limit as $\Delta x \to 0$. In reality we are concerned with obtaining admissable solutions on a relatively coarse mesh.

In order to arrive at a proper criterion, Harten examines the Riemann initial value problem [23] for Eq 1.1:

$$\begin{aligned} u(x,0) = \phi(x) &= u_L \quad x < 0 \\ &= u_R \quad x > 0 \end{aligned} \tag{1.48}$$

with u_L and u_R satisfying the Rankine-Hugoniot relations with wave speed s. If $u(x,t) = \phi(x - st)$ is to satisfy Oleinik's inequality the numerical scheme must yield a steady progressing profile with a narrow transition from u_L to u_R [21, 23]. Harten refers to this property as *resolution.*

If the solution $u(x,t) = \phi(x - st)$ is inadmissable, then the solution is a fan of waves [23]. This fan of waves is a function of x/t and consists of a rarefaction, or expansion, wave in the same field as the initial discontinuity. The physical solution requires the initial discontinuity break up instantaeously, since $u(x,t) = \phi(x/t)$.The term *entropy enforcement* refers to the requirement that the numerical scheme break

up the initial discontinuity at a *fast* rate, thus imitating the physical behavior [23].

The systems of conservation laws under consideration contain two types of characteristic fields, termed nonlinear and linearly degenerate by Harten [23]. The nonlinear fields are defined such that $a_u^k R^k \neq 0$, while the linearly degenerate fields are defined by $a_u^k R^k \equiv 0$. The waves of a nonlinear field are shock waves or expansion waves while the waves of a linearly degenerate field are solely contact, or entropy, discontinuities.

To address the question of entropy enforcement, consider the scheme given by Eq 1.26, which has the effective numerical viscosity coefficient

$$\beta(u,\lambda) = \frac{1}{2}\left[Q(\nu) - \nu^2\right] \tag{1.49}$$

The least dissipative form of Q is arrived at by choosing it to be consistent with Eq 1.29 such that

$$Q(x) = |x| \tag{1.50}$$

With Q given by Eq 1.50, the scheme of Eq 1.26 can be rewritten as [23]

$$v_j^{n+1} = v_j^n - \left(\bar{\nu}_{j+1/2}\right)^- \Delta_{j+1/2} v^n - \left(\bar{\nu}_{j-1/2}\right)^+ \Delta_{j-1/2} v^n \tag{1.51}$$

where

$$\nu^- = \min(\nu, 0) = \tfrac{1}{2}\left(\nu - |\nu|\right) \qquad \nu^+ = \max(\nu, 0) = \tfrac{1}{2}\left(\nu + |\nu|\right) \tag{1.52}$$

Harten points out that the scheme of Eqs 1.51 and 1.52 is a generalization of the Courant, Isaacson, and Rees scheme, which has been thoroughly analyzed in the literature. The interested reader is referred to reference [23] for further details.

If the scheme given by Eqs 1.51 and 1.52 is applied to the Riemann problem with the Rankine-Hugoniot relation satisfied by letting the speed of propagation be

zero, Eq 1.51 holds the initial discontinuity steady regardless of entropy considerations. In other words, the initial discontinuity is not broken up and there is no entropy enforcement in this case.

The problem is that the numerical viscosity vanishes for $\nu = 0$. Harten eliminates this problem by modifying $Q(x) = |x|$ near $x = 0$ to be positive. The modification is as follows [23] for $0 < \epsilon \leq \frac{1}{2}$

$$\begin{aligned} Q(x) &= (x^2/(4\epsilon)) + \epsilon \quad |x| < 2\epsilon \\ &= \quad |x| \quad\quad\quad |x| \geq 2\epsilon \end{aligned} \tag{1.53}$$

with the entropy correction parameter, ϵ, typically of order 0.1.

Harten summarizes the results of numerical experiments carried out with the scheme of Eqs 1.44 and 1.45 applied to the Euler equations for the Riemann problem. These experiments used $\epsilon = 0.05$, 0.1, and 0.25 for all fields, and also $\epsilon = 0$ for the linearly degenerate field. Basically, highly resolved shocks were obtained for all values of ϵ under consideration. The contact surface was better resolved than with the first-order accurate scheme of Eqs 1.51 and 1.52, but still remained rather smeared.

To prevent excessive smearing in the linearly degenerate field containing the contact surface, Harten replaces Eq 1.46 in the linearly degenerate field with [23]

$$g_j = \bar{g}_j + \theta_j \bar{\bar{g}}_j \tag{1.54}$$

where $\bar{g}_j$ is the right hand side of g_j given by Eq 1.46 and, $\bar{\bar{g}}_j$ is

$$\bar{\bar{g}}_j = S \max\left[0, \min\left(S\sigma_{j-1/2}\alpha_{j-1/2}, \sigma_{j+1/2}\left|\alpha_{j+1/2}\right|\right)\right] \tag{1.55}$$

with

$$S = sgn\left(\alpha_{j+1/2}\right) \tag{1.56}$$

$$\sigma_{j+1/2} = \sigma_{j+1/2}\left(\nu_{j+1/2}\right) = \frac{1}{2}\left[1 - Q\left(\nu_{j+1/2}\right)\right] \tag{1.57}$$

$$\theta_j = \left|\alpha_{j+1/2} - \alpha_{j-1/2}\right| / \left(\left|\alpha_{j+1/2}\right| + \left|\alpha_{j-1/2}\right|\right) \tag{1.58}$$

II. Analysis

2.1 Euler Equations

The Euler equations are statements of the conservation laws for mass, momentum, and energy assuming an inviscid, nonconducting gas. When the Euler equations are arranged such that ρ, ρu, ρv, and e are the dependent variables the conservative or divergence form is obtained. Lax showed that the conservative form of the Euler equations satisfies the weak solution of the Rankine-Hugoniot relations and thus correctly predicts the jump conditions across the shock discontinuity [1, 34]. In fact, use of the conservative form is necessary for the discontinuity to represent a physical wave when shock capturing schemes are applied [1]. The conservative form is often referred to as the divergence form because the equations identify the divergence of physical quantities. The governing equations may be written in the following vector form:

$$\frac{\partial U}{\partial t} + \frac{\partial F(U)}{\partial x} + \frac{\partial G(U)}{\partial y} = 0 \tag{2.1}$$

where U contains the dependent variables which are the density, ρ; x-momentum, ρu; y-momentum, ρv; and total energy per unit volume, e. F contains the flux terms differentiated with respect to x, and G contains the flux terms differentiated with respect to y. The elements of U, F, and G are:

$$U = \begin{bmatrix} \rho \\ m \\ n \\ e \end{bmatrix} \quad F = \begin{bmatrix} m \\ m^2/\rho + p \\ mv \\ (e+p)m/\rho \end{bmatrix} \quad G = \begin{bmatrix} n \\ nu \\ n^2/\rho + p \\ (e+p)n/\rho \end{bmatrix} \tag{2.2}$$

where $m = \rho u$ and $n = \rho v$. The pressure, p, is given as

$$p = (\gamma - 1)\left[e - \frac{(m^2 + n^2)}{2\rho}\right] \tag{2.3}$$

for a thermally and calorically perfect gas.

A general spatial transformation of the form $\xi = \xi(x, y)$ and $\eta = \eta(x, y)$ is used to transform Eq 2.1 from the physical domain (x, y) to the computational domain (ξ, η). The strong conservation law form of the Euler equations is now given by [42]

$$\frac{\partial \hat{U}}{\partial t} + \frac{\partial \hat{F}(\hat{U})}{\partial \xi} + \frac{\partial \hat{G}(\hat{U})}{\partial \eta} = 0 \tag{2.4}$$

$$\hat{U} = U/J \tag{2.5}$$

$$\hat{F} = \left(\xi_x F + \xi_y G\right)/J \tag{2.6}$$

$$\hat{G} = \left(\eta_x F + \eta_y G\right)/J \tag{2.7}$$

$$J = \xi_x \eta_y - \xi_y \eta_x \tag{2.8}$$

where J is the Jacobian of the transformation.

Since the TVD method used herein utilizes the local-characteristic approach, which is a generalization of Roe's approximate Riemann solver[35], the Jacobians $\hat{A}$ and $\hat{B}$ of $\hat{F}$ and $\hat{G}$ are required and can be written as

$$\hat{A} = \left(\xi_x A + \xi_y B\right) \tag{2.9}$$

$$\hat{B} = \left(\eta_x A + \eta_y B\right) \tag{2.10}$$

where

$$A = F_U = \begin{bmatrix} 0 & 1 & 0 & 0 \\ \frac{1}{2}(\gamma-1)\left(u^2+v^2\right) - u^2 & (3-\gamma)u & (1-\gamma)v & \gamma - 1 \\ -uv & v & u & 0 \\ \left[\frac{1}{2}(\gamma-1)\left(u^2+v^2\right) - H\right]u & H - (\gamma-1)u^2 & (1-\gamma)uv & \gamma u \end{bmatrix}$$

$$B = G_U = \begin{bmatrix} 0 & 0 & 1 & 0 \\ -uv & v & u & 0 \\ \frac{1}{2}(\gamma-1)\left(u^2+v^2\right)-v^2 & (1-\gamma)u & (3-\gamma)v & \gamma-1 \\ \left[\left(\frac{1}{2}\gamma-1\right)\left(u^2+v^2\right)-H\right]v & (1-\gamma)uv & H-(\gamma-1)v^2 & \gamma v \end{bmatrix}$$

with the total enthalpy, H, given by

$$H = \frac{\gamma p}{(\gamma-1)\rho} + \frac{1}{2}\left(u^2+v^2\right) \tag{2.11}$$

The eigenvalues of $\hat{A}$, denoted $\left(a_\xi^1, a_\xi^2, a_\xi^3, a_\xi^4\right)$, are

$$a_\xi = \begin{pmatrix} \xi_x u + \xi_y v - k_\xi c \\ \xi_x u + \xi_y v \\ \xi_x u + \xi_y v + k_\xi c \\ \xi_x u + \xi_y v \end{pmatrix} \tag{2.12}$$

where

$$k_\xi = \sqrt{\xi_x^2 + \xi_y^2} \tag{2.13}$$

The right eigenvectors of $\hat{A}$, $\left(R_\xi^1, R_\xi^2, R_\xi^3, R_\xi^4\right)$, are

$$R_\xi^1 = \begin{bmatrix} 1 \\ u - k_1 c \\ v - k_2 c \\ H - k_1 uc - k_2 vc \end{bmatrix} \quad R_\xi^2 = \begin{bmatrix} 1 \\ u \\ v \\ \frac{1}{2}(u^2+v^2) \end{bmatrix}$$

$$R_\xi^3 = \begin{bmatrix} 1 \\ u + k_1 c \\ v + k_2 c \\ H + k_1 uc + k_2 vc \end{bmatrix} \quad R_\xi^4 = \begin{bmatrix} 0 \\ -k_2 \\ k_1 \\ k_1 v - k_2 u \end{bmatrix} \tag{2.14}$$

where

$$k_1 = \left[\frac{\xi_x}{J} \Big/ \sqrt{\left(\frac{\xi_x}{J}\right)^2 + \left(\frac{\xi_y}{J}\right)^2} \right] \tag{2.15}$$

and

$$k_2 = \left[\frac{\xi_y}{J} \Big/ \sqrt{\left(\frac{\xi_x}{J}\right)^2 + \left(\frac{\xi_y}{J}\right)^2} \right] \tag{2.16}$$

The eigenvalues and eigenvectors of $\hat{B}$ are obtained by replacing ξ in Eqs 2.12 through 2.16 with η:

$$a_\eta = \begin{pmatrix} \eta_x u + \eta_y v - k_\eta c \\ \eta_x u + \eta_y v \\ \eta_x u + \eta_y v + k_\eta c \\ \eta_x u + \eta_y v \end{pmatrix} \tag{2.17}$$

$$k_\eta = \sqrt{\eta_x^2 + \eta_y^2} \tag{2.18}$$

$$R_\eta^1 = \begin{bmatrix} 1.0 \\ u - k_1 c \\ v - k_2 c \\ H - k_1 u c - k_2 v c \end{bmatrix} \quad R_\eta^2 = \begin{bmatrix} 1.0 \\ u \\ v \\ \frac{1}{2}(u^2 + v^2) \end{bmatrix} \tag{2.19}$$

$$R_\eta^3 = \begin{bmatrix} 1.0 \\ u + k_1 c \\ v + k_2 c \\ H + k_1 u c + k_2 v c \end{bmatrix} \quad R_\eta^4 = \begin{bmatrix} 0.0 \\ -k_2 \\ k_1 \\ k_1 v - k_2 u \end{bmatrix}$$

$$k_1 = \left[\frac{\eta_x}{J} \Big/ \sqrt{\left(\frac{\eta_x}{J}\right)^2 + \left(\frac{\eta_y}{J}\right)^2} \right] \tag{2.20}$$

$$k_2 = \left[\frac{\eta_y}{J} \Big/ \sqrt{\left(\frac{\eta_x}{J}\right)^2 + \left(\frac{\eta_y}{J}\right)^2} \right] \tag{2.21}$$

2.2 Numerical Procedure

2.2.1 2-D Harten-Yee Finite-Volume Algorithm. An upwind TVD scheme in finite-volume form [42] is used in the present study. The grid spacing is denoted by $\Delta\xi$ and $\Delta\eta$, such that $\xi = j\Delta\xi$ and $\eta = k\Delta\eta$. Utilizing the Strang-type fractional step method allows the scheme to be implemented in a local-characteristic approach and ensures second-order accuracy:

$$\hat{U}^{n+2}_{j,k} = \mathcal{L}^{h/2}_{\xi}\mathcal{L}^{h}_{\eta}\mathcal{L}^{h}_{\xi}\mathcal{L}^{h}_{\eta}\mathcal{L}^{h/2}_{\xi}\hat{U}^{n}_{j,k} \tag{2.22}$$

where

$$\mathcal{L}^{h}_{\xi}\hat{U}^{n}_{j,k} = \hat{U}^{*}_{j,k} = \hat{U}^{n}_{j,k} - \frac{\Delta t}{\Delta\xi}\left(\tilde{F}^{n}_{j+\frac{1}{2},k} - \tilde{F}^{n}_{j-\frac{1}{2},k}\right) \tag{2.23}$$

$$\mathcal{L}^{h}_{\eta}\hat{U}^{*}_{j,k} = \hat{U}^{*}_{j,k} - \frac{\Delta t}{\Delta\eta}\left(\tilde{G}^{*}_{j,k+\frac{1}{2}} - \tilde{G}^{*}_{j,k-\frac{1}{2}}\right) \tag{2.24}$$

with $h = \Delta t$. Application of the entire sequence of operators (one iteration) advances the solution two time levels. The functions $\tilde{F}_{j+\frac{1}{2},k}$ and $\tilde{G}_{j,k+\frac{1}{2}}$ are the numerical fluxes in the ξ and η directions evaluated at cell interfaces. For instance, $\tilde{F}_{j+\frac{1}{2},k}$ in Yee's finite-volume formulation is expressed as

$$\begin{aligned}\tilde{F}_{j+\frac{1}{2},k} \;=\; \tfrac{1}{2}\Big[&\left(\tfrac{\xi_x}{J}\right)_{j+\frac{1}{2}}(F_{j,k}+F_{j+1,k}) + \left(\tfrac{\xi_y}{J}\right)_{j+\frac{1}{2}}(G_{j,k}+G_{j+1,k}) \\ &+\tfrac{\Delta\xi}{\Delta t}R_{\xi_{j+\frac{1}{2}}}\Phi_{j+\frac{1}{2}}/J_{j+\frac{1}{2}}\Big]\end{aligned} \tag{2.25}$$

where the subscript $j+\frac{1}{2}$ is a simplified notation for $j+\frac{1}{2},k$. The numerical flux function in the η direction is defined similarly:

$$\begin{aligned}\tilde{G}_{j,k+\frac{1}{2}} \;=\; \tfrac{1}{2}\Big[&\left(\tfrac{\eta_x}{J}\right)_{k+\frac{1}{2}}(F_{j,k}+F_{j,k+1}) + \left(\tfrac{\eta_y}{J}\right)_{k+\frac{1}{2}}(G_{j,k}+G_{j,k+1}) \\ &+\tfrac{\Delta\eta}{\Delta t}R_{\eta_{k+\frac{1}{2}}}\Phi_{k+\frac{1}{2}}/J_{k+\frac{1}{2}}\Big]\end{aligned} \tag{2.26}$$

The eigenvalues and eigenvectors are evaluated at cell interfaces using symmetric averages of $U_{j,k}$ and $U_{j+1,k}$, $U_{j,k}$ and $U_{j,k+1}$, respectively. Roe's averaging

technique for a perfect gas is used herein and takes the form [35]

$$u_{j+\frac{1}{2},k} = \frac{\bar{D}u_{j+1,k} + u_{j,k}}{\bar{D}+1} \tag{2.27}$$

$$v_{j+\frac{1}{2},k} = \frac{\bar{D}v_{j+1,k} + v_{j,k}}{\bar{D}+1} \tag{2.28}$$

$$H_{j+\frac{1}{2},k} = \frac{\bar{D}H_{j+1,k} + H_{j,k}}{\bar{D}+1} \tag{2.29}$$

$$c^2_{j+\frac{1}{2},k} = (\gamma-1)\left[H_{j+\frac{1}{2},k} - \frac{1}{2}\left(u^2_{j+\frac{1}{2},k} + v^2_{j+\frac{1}{2},k}\right)\right] \tag{2.30}$$

where

$$\bar{D} = \sqrt{\rho_{j+1,k}/\rho_{j,k}} \tag{2.31}$$

Roe's averaging technique is used because it has the computational advantage of perfectly resolving stationary [43], but not necessarily moving, discontinuities.

The quantities $\left(\frac{\xi_x}{J}\right)_{j+\frac{1}{2}}$ and $1/J_{j+\frac{1}{2}}$ are defined as follows for the finite-volume formulation

$$\left(\frac{\xi_x}{J}\right)_{j+\frac{1}{2}} = \frac{1}{2}\left[\left(\frac{\xi_x}{J}\right)_{j,k} + \left(\frac{\xi_x}{J}\right)_{j+1,k}\right] \tag{2.32}$$

$$\frac{1}{J_{j+\frac{1}{2}}} = \frac{1}{2}\left(\frac{1}{J_{j+1,k}} + \frac{1}{J_{j,k}}\right) \tag{2.33}$$

The constants $(k_1)_{j+\frac{1}{2}}$ and $(k_2)_{j+\frac{1}{2}}$ necessary in determining $R_{\xi_{j+\frac{1}{2}}}$, Eq 2.15, are defined as

$$(k_1)_{j+\frac{1}{2}} = \frac{\left(\frac{\xi_x}{J}\right)_{j+\frac{1}{2}}}{\sqrt{\left(\frac{\xi_x}{J}\right)^2_{j+\frac{1}{2}} + \left(\frac{\xi_y}{J}\right)^2_{j+\frac{1}{2}}}} \tag{2.34}$$

and

$$(k_2)_{j+\frac{1}{2}} = \frac{\left(\frac{\xi_y}{J}\right)_{j+\frac{1}{2}}}{\sqrt{\left(\frac{\xi_x}{J}\right)^2_{j+\frac{1}{2}} + \left(\frac{\xi_y}{J}\right)^2_{j+\frac{1}{2}}}} \tag{2.35}$$

The vector function $\Phi_{j+\frac{1}{2}}$ is composed of elements denoted as $\left(\phi^l_{j+\frac{1}{2}}\right)^U$ for a second-order upwind TVD scheme. The elements are given by

$$\phi^l_{j+\frac{1}{2}} = \sigma\left(\nu^l_{j+\frac{1}{2}}\right)\left(g^l_{j+1} + g^l_j\right) - Q\left(\nu^l_{j+\frac{1}{2}} + \gamma^l_{j+\frac{1}{2}}\right)\alpha^l_{j+\frac{1}{2}} \tag{2.36}$$

where, with $\lambda = \Delta t/\Delta\xi$

$$\nu^l_{j+\frac{1}{2}} = \lambda a^l_{j+\frac{1}{2}} \tag{2.37}$$

$\alpha_{j+\frac{1}{2}}$ is the difference of the characteristic variables in the ξ direction,

$$\alpha_{j+\frac{1}{2}} = R^{-1}_{j+\frac{1}{2}}\left(U_{j+1,k} - U_{j,k}\right) \tag{2.38}$$

or

$$\begin{bmatrix} \alpha^1_{j+\frac{1}{2}} \\ \alpha^2_{j+\frac{1}{2}} \\ \alpha^3_{j+\frac{1}{2}} \\ \alpha^4_{j+\frac{1}{2}} \end{bmatrix} = \begin{bmatrix} (aa - bb)/2 \\ \Delta_{j+\frac{1}{2}}\rho - aa \\ (aa + bb)/2 \\ cc \end{bmatrix} \tag{2.39}$$

where

$$aa = \frac{\gamma - 1}{c^2_{j+\frac{1}{2}}}\left[\Delta_{j+\frac{1}{2}}e + \frac{u^2_{j+\frac{1}{2}} + v^2_{j+\frac{1}{2}}}{2}\Delta_{j+\frac{1}{2}}\rho - u_{j+\frac{1}{2}}\Delta_{j+\frac{1}{2}}m - v_{j+\frac{1}{2}}\Delta_{j+\frac{1}{2}}n\right] \tag{2.40}$$

$$bb = \frac{1}{c_{j+\frac{1}{2}}}\left[k_1\Delta_{j+\frac{1}{2}}m - \left(k_1u_{j+\frac{1}{2}} + k_2v_{j+\frac{1}{2}}\right)\Delta_{j+\frac{1}{2}}\rho + k_2\Delta_{j+\frac{1}{2}}n\right] \tag{2.41}$$

$$cc = k_1\Delta_{j+\frac{1}{2}}n + \left(k_2u_{j+\frac{1}{2}} - k_1v_{j+\frac{1}{2}}\right)\Delta_{j+\frac{1}{2}}\rho - k_2\Delta_{j+\frac{1}{2}}m \tag{2.42}$$

$$\Delta_{j+\frac{1}{2}}z = z_{j+1,k} - z_{j,k} \tag{2.43}$$

The difference of the local characteristic variables in the η direction is obtained in similar fashion:

$$\alpha_{k+\frac{1}{2}} = R^{-1}_{k+\frac{1}{2}}\left(U_{j,k+1} - U_{j,k}\right) \tag{2.44}$$

$$\begin{bmatrix} \alpha^1_{k+\frac{1}{2}} \\ \alpha^2_{k+\frac{1}{2}} \\ \alpha^3_{k+\frac{1}{2}} \\ \alpha^4_{k+\frac{1}{2}} \end{bmatrix} = \begin{bmatrix} (dd-ee)/2 \\ \Delta_{k+\frac{1}{2}}\rho - aa \\ (dd+ee)/2 \\ ff \end{bmatrix} \tag{2.45}$$

where

$$dd = \frac{\gamma-1}{c^2_{k+\frac{1}{2}}}\left[\Delta_{k+\frac{1}{2}}e + \frac{u^2_{k+\frac{1}{2}}+v^2_{k+\frac{1}{2}}}{2}\Delta_{k+\frac{1}{2}}\rho - u_{k+\frac{1}{2}}\Delta_{k+\frac{1}{2}}m - v_{k+\frac{1}{2}}\Delta_{k+\frac{1}{2}}n\right] \tag{2.46}$$

$$ee = \frac{1}{c_{k+\frac{1}{2}}}\left[k_1\Delta_{k+\frac{1}{2}}m - \left(k_1u_{k+\frac{1}{2}} + k_2v_{k+\frac{1}{2}}\right)\Delta_{k+\frac{1}{2}}\rho + k_2\Delta_{k+\frac{1}{2}}n\right] \tag{2.47}$$

$$ff = k_1\Delta_{k+\frac{1}{2}}n + \left(k_2u_{k+\frac{1}{2}} - k_1v_{k+\frac{1}{2}}\right)\Delta_{k+\frac{1}{2}}\rho - k_2\Delta_{k+\frac{1}{2}}m \tag{2.48}$$

with

$$(k_1)_{k+\frac{1}{2}} = \frac{\left(\frac{\eta_x}{J}\right)_{k+\frac{1}{2}}}{\sqrt{\left(\frac{\eta_x}{J}\right)^2_{k+\frac{1}{2}} + \left(\frac{\eta_y}{J}\right)^2_{k+\frac{1}{2}}}} \tag{2.49}$$

$$(k_2)_{k+\frac{1}{2}} = \frac{\left(\frac{\eta_y}{J}\right)_{k+\frac{1}{2}}}{\sqrt{\left(\frac{\eta_x}{J}\right)^2_{k+\frac{1}{2}} + \left(\frac{\eta_y}{J}\right)^2_{k+\frac{1}{2}}}} \tag{2.50}$$

$$\Delta_{k+\frac{1}{2}}z = z_{j,k+1} - z_{j,k} \tag{2.51}$$

The function $\gamma^l_{j+\frac{1}{2}}$ is given by

$$\gamma^l_{j+\frac{1}{2}} = \begin{cases} \sigma\left(\lambda a^l_{j+\frac{1}{2}}\right)\frac{\left(g^l_{j+1}-g^l_j\right)}{\alpha^l_{j+\frac{1}{2}}} & \left(\alpha^l_{j+\frac{1}{2}} \neq 0\right) \\ 0 & \left(\alpha^l_{j+\frac{1}{2}} = 0\right) \end{cases} \tag{2.52}$$

where

$$\sigma(x) = \frac{1}{2}\left[Q(x) - x^2\right] \tag{2.53}$$

and

$$Q(x) = \begin{cases} |x| & (|x| \geq 2\epsilon) \\ (x^2/(4\epsilon)) + \epsilon & (|x| < 2\epsilon) \end{cases} \tag{2.54}$$

The entropy correction parameter, ϵ, is generally fixed during computations, but can vary between 0 and 0.5.

The function g_j^l in Eq 2.36, initially referred to in Section 1.2.2, is termed the 'limiter' function and can be expressed in a variety of ways [42]. The present study bases the choice of the limiter on the type of characteristic field under consideration. For the nonlinear fields, $a^l R^l \neq 0$, Eq 4.34d of Yee [42] is used:

$$g_j^l = \left(\alpha_{j+\frac{1}{2}}^l \alpha_{j-\frac{1}{2}}^l + \left|\alpha_{j+\frac{1}{2}}^l \alpha_{j-\frac{1}{2}}^l\right|\right) / \left(\alpha_{j+\frac{1}{2}}^l + \alpha_{j-\frac{1}{2}}^l\right) \tag{2.55}$$

For the linearly degenerate fields, $a^l R^l \equiv 0$, Eq 4.34g of Yee [42] is applied:

$$g_j^l = S \cdot \max\left[0, \min\left(2\left|\alpha_{j+\frac{1}{2}}^l\right|, S \cdot \alpha_{j-\frac{1}{2}}^l\right), \min\left(\left|\alpha_{j+\frac{1}{2}}^l\right|, 2S \cdot \alpha_{j-\frac{1}{2}}^l\right)\right] \tag{2.56}$$

where

$$S = sgn\left(\alpha_{j+\frac{1}{2}}^l\right) \tag{2.57}$$

The nonlinear fields correspond to $l = 1$ and $l = 3$ while the linearly degenerate fields correspond to $l = 2$ and $l = 4$. It should again be noted that the waves of a nonlinear field are either shocks or rarefraction waves while the waves of a linearly degenerate field are uniquely contact discontinuities [23]. Since this is a five-point scheme, the values of g_j^l are needed at cell centers just outside the computational domain. Zeroth-order extrapolation is used to obtain the necessary values, following the example of Harten [23].

2.2.2 2-D Harten-Yee Chain-Rule Algorithm. In addition to the finite-volume formulation of Yee, a finite-difference form based on the chain-rule con-

servation form of the governing equations was utilized [38]:

$$\frac{\partial U}{\partial t} + \xi_x \frac{\partial F(U)}{\partial \xi} + \xi_y \frac{\partial G(U)}{\partial \xi} + \eta_x \frac{\partial F(U)}{\partial \eta} + \eta_y \frac{\partial G(U)}{\partial \eta} = 0 \tag{2.58}$$

Previous researchers report that the governing equations in this form are more computationally efficient than the strong conservation form used in the finite-volume approach [38]. This was found not to be the case for the current TVD algorithms, with both formulations performing approximately the same in terms of computational efficiency.

The local characteristic approach given by Eq 2.22 is now applied to U instead of $\hat{U}$:

$$U_{j,k}^{n+2} = \mathcal{L}_\xi^{h/2} \mathcal{L}_\eta^h \mathcal{L}_\xi^h \mathcal{L}_\eta^h \mathcal{L}_\xi^{h/2} U_{j,k}^n \tag{2.59}$$

where

$$\mathcal{L}_\xi^h U_{j,k}^n = U_{j,k}^* = U_{j,k}^n - \frac{\Delta t}{\Delta \xi} \left(\tilde{F}_{j+\frac{1}{2},k}^n - \tilde{F}_{j-\frac{1}{2},k}^n \right) \tag{2.60}$$

$$\mathcal{L}_\eta^h U_{j,k}^* = U_{j,k}^* - \frac{\Delta t}{\Delta \eta} \left(\tilde{G}_{j,k+\frac{1}{2}}^* - \tilde{G}_{j,k-\frac{1}{2}}^* \right) \tag{2.61}$$

The numerical fluxes, $\tilde{F}_{j+\frac{1}{2},k}$ and $\tilde{G}_{j,k+\frac{1}{2}}$, for the chain-rule conservation form are

$$\tilde{F}_{j+\frac{1}{2},k} = \frac{1}{2} \left[(\xi_x)_{j,k} (F_{j,k} + F_{j+1,k}) + (\xi_y)_{j,k} (G_{j,k} + G_{j+1,k}) + \frac{\Delta \xi}{\Delta t} R_{\xi_{j+\frac{1}{2}}} \Phi_{j+\frac{1}{2}} \right] \tag{2.62}$$

and

$$\tilde{G}_{j,k+\frac{1}{2}} = \frac{1}{2} \left[(\eta_x)_{j,k} (F_{j,k} + F_{j,k+1}) + (\eta_y)_{j,k} (G_{j,k} + G_{j,k+1}) + \frac{\Delta \eta}{\Delta t} R_{\eta_{k+\frac{1}{2}}} \Phi_{k+\frac{1}{2}} \right] \tag{2.63}$$

The quantities $(\xi_x)_{j+\frac{1}{2}}$, $(k_1)_{j+\frac{1}{2}}$, and $(k_2)_{j+\frac{1}{2}}$ are defined as follows for the chain rule formulation:

$$(\xi_x)_{j+\frac{1}{2}} = \frac{1}{2} \left[(\xi_x)_{j,k} + (\xi_x)_{j+1,k} \right] \tag{2.64}$$

$$(k_1)_{j+\frac{1}{2}} = \frac{(\xi_x)_{j+\frac{1}{2}}}{\sqrt{(\xi_x)^2_{j+\frac{1}{2}} + (\xi_y)^2_{j+\frac{1}{2}}}} \tag{2.65}$$

$$(k_2)_{j+\frac{1}{2}} = \frac{(\xi_y)_{j+\frac{1}{2}}}{\sqrt{(\xi_x)^2_{j+\frac{1}{2}} + (\xi_y)^2_{j+\frac{1}{2}}}} \tag{2.66}$$

2.3 Navier-Stokes Equations

The conservative form of the Navier-Stokes equations is written as

$$\frac{\partial U}{\partial t} + \frac{\partial F(U)}{\partial x} + \frac{\partial G(U)}{\partial y} = \frac{\partial F_v(U, U_x, U_y)}{\partial x} + \frac{\partial G_v(U, U_x, U_y)}{\partial y} \tag{2.67}$$

where U, F, and G are the same as for the Euler equations, Eq 2.1. F_v and G_v are the viscous flux terms, given as

$$F_v = \begin{bmatrix} 0 \\ \tau_{xx} \\ \tau_{xy} \\ u\tau_{xx} + v\tau_{xy} - q_x \end{bmatrix} \quad G_v = \begin{bmatrix} 0 \\ \tau_{xy} \\ \tau_{yy} \\ u\tau_{xy} + v\tau_{yy} - q_y \end{bmatrix} \tag{2.68}$$

τ_{xx}, τ_{xy}, and τ_{yy} are the viscous stresses:

$$\begin{aligned} \tau_{xx} &= (2\mu + \lambda)u_x + \lambda v_y \\ \tau_{xy} &= \mu\,(u_y + v_x) \\ \tau_{yy} &= (2\mu + \lambda)v_y + \lambda u_x \end{aligned} \tag{2.69}$$

where μ and λ are the first and second coefficients of viscosity respectively. The first coefficient of viscosity is determined using Sutherland's formula [1];

$$\mu = C_1 \frac{T^{3/2}}{T + C_2} \tag{2.70}$$

where $C_1 = 1.458 \times 10^{-6}\ kg/\left(m \cdot s \cdot \sqrt{K}\right)$ and $C_2 = 110.4\ K$. The second coefficient of viscosity is given by

$$B = 2 + \frac{\lambda}{\mu} \tag{2.71}$$

where $B = 4/3$ yields Stoke's hypothesis, $\lambda = -2/3\mu$. Solutions were also arrived at using $B = 2$, based on Sherman's work as reported by White [45]. No difference was observed in the numerical solutions using $B = 4/3$ or $B = 2$.

The quantities q_x and q_y are components of the heat flux vector, $q = -k\nabla T$. The coefficient of thermal conductivity, k, is determined from the Prandtl number, Pr:

$$Pr = \frac{\mu C_p}{k} \tag{2.72}$$

with $Pr = 0.72$ for air.

The equations may be written in linearized form as

$$U_t + AU_x + BU_y = A_1 U_x + B_1 U_y + A_2 U_{xx} + B_2 U_{yy} + (A_3 + B_3)\, U_{xy} \tag{2.73}$$

where the viscous Jacobian matrices are

$$\begin{aligned} A_1 &= \partial F_v/\partial U \quad A_2 = \partial F_v/\partial U_x \quad A_3 = \partial F_v/\partial U_y \\ B_1 &= \partial G_v/\partial U \quad B_2 = \partial G_v/\partial U_y \quad B_3 = \partial G_v/\partial U_x \end{aligned} \tag{2.74}$$

with the individual terms given in Appendix A.

A general spatial transformation of the form $\xi = \xi(x, y)$ and $\eta = \eta(x, y)$ is used to transform Eq 2.73 from the physical domain (x, y) to the computational domain (ξ, η):

$$U_t + \hat{A}U_\xi + \hat{B}U_\eta = \hat{A}_1 U_\xi + \hat{B}_1 U_\eta + \hat{A}_2 U_{\xi\xi} + \hat{B}_2 U_{\eta\eta} + \left(\hat{A}_3 + \hat{B}_3\right) U_{\xi\eta} \tag{2.75}$$

where

$$\begin{aligned}
\hat{A} &= \xi_x A + \xi_y B \\
\hat{A}_1 &= \xi_x A_1 + \xi_y B_1 \\
\hat{A}_2 &= \xi_x^2 A_2 + \xi_y^2 B_2 + \xi_x \xi_y \left(A_3 + B_3\right) \\
\hat{A}_3 &= \xi_x \eta_y A_3 + \xi_y \eta_x B_3 + \xi_x \eta_x A_2 + \xi_y \eta_y B_2
\end{aligned} \tag{2.76}$$

and

$$\begin{aligned}
\hat{B} &= \eta_x A + \eta_y B \\
\hat{B}_1 &= \eta_x A_1 + \eta_y B_1 \\
\hat{B}_2 &= \eta_x^2 A_2 + \eta_y^2 B_2 + \eta_x \eta_y \left(A_3 + B_3\right) \\
\hat{B}_3 &= \xi_x \eta_y B_3 + \xi_y \eta_x A_3 + \xi_x \eta_x A_2 + \xi_y \eta_y B_2
\end{aligned} \tag{2.77}$$

2.4 Numerical Procedure

A first-order time, second-order space, upwind TVD scheme is now presented for the Navier-Stokes equations. Based upon the excellent results achieved in the inviscid case, a chain-rule formulation is utilized. The scheme for the Euler equations , described in Section 2.2.2, is second-order accurate in space and time. Taylor series expansion shows the scheme is a representation of

$$\begin{aligned}
U_t + \xi_x F_\xi + \eta_x F_\eta + \xi_y G_\xi + \eta_y G_\eta &= \tfrac{\Delta t}{2}\left[-U_{tt} + \hat{A}^2 U_{\xi\xi} + \left(\hat{A}\hat{B} + \hat{B}\hat{A}\right) U_{\xi\eta}\right. \\
&\quad \left. + \hat{B}^2 U_{\eta\eta}\right] + O\left[\Delta t^2, \Delta\xi^2, \Delta\eta^2\right]
\end{aligned} \tag{2.78}$$

and is second-order accurate for the Euler equations, since

$$U_{tt} = \hat{A}^2 U_{\xi\xi} + \left(\hat{A}\hat{B} + B\hat{A}\right) U_{\xi\eta} + \hat{B}^2 U_{\eta\eta} \tag{2.79}$$

Viscous terms are added to the Euler scheme, Eqs 2.60 and 2.61, using second-order accurate, central-difference approximations:

$$\mathcal{L}_\xi^h U_{j,k}^n = U_{j,k}^* = U_{j,k}^n - \frac{\Delta t}{\Delta \xi}\left(\tilde{F}_{j+\frac{1}{2},k}^n - \tilde{F}_{j-\frac{1}{2},k}^n\right) + \Delta t \Psi_\xi^n \tag{2.80}$$

$$\mathcal{L}_\eta^h U_{j,k}^* = U_{j,k}^* - \frac{\Delta t}{\Delta \eta}\left(\tilde{G}_{j,k+\frac{1}{2}}^* - \tilde{G}_{j,k-\frac{1}{2}}^*\right) + \Delta t \Psi_\eta^* \tag{2.81}$$

where $\tilde{F}$ and $\tilde{G}$ are given by Eqs 2.62 and 2.63. The viscous terms, Ψ_ξ and Ψ_η, are

$$\Psi_\xi = \frac{1}{2\Delta\xi}\left[(\xi_x)_{j,k}\left(F_{v_{j+1,k}} - F_{v_{j,k}}\right) + (\xi_y)_{j,k}\left(G_{v_{j+1,k}} - G_{v_{j,k}}\right)\right] \tag{2.82}$$

and

$$\Psi_\eta = \frac{1}{2\Delta\eta}\left[(\eta_x)_{j,k}\left(F_{v_{j,k+1}} - F_{v_{j,k}}\right) + (\eta_y)_{j,k}\left(G_{v_{j,k+1}} - G_{v_{j,k}}\right)\right] \tag{2.83}$$

In order to maintain second-order accuracy, the derivatives appearing in the viscous terms of F_v and G_v must be differenced appropriately. The ζ derivative terms in F_v and G_v are backward differenced when computing Ψ_ζ. Similarly, the η derivative terms in F_v and G_v are backward differenced when computing Ψ_η. All other derivative terms are central differenced.

The scheme given by Eqs 2.80 through 2.83 is a representation of

$$\begin{aligned} U_t + \xi_x F_\xi + \eta_x F_\eta + \xi_y G_\xi + \eta_y G_\eta \;=\; & \xi_x F_{v_\xi} + \eta_x F_{v_\eta} + \xi_y G_{v_\xi} + \eta_y G_{v_\eta} \\ & + \tfrac{\Delta t}{2}\left[-U_{tt} + \hat{A}^2 U_{\xi\xi} + \left(\hat{A}\hat{B} + \hat{B}\hat{A}\right) U_{\xi\eta}\right. \\ & \left. + \hat{B}^2 U_{\eta\eta}\right] + O\left[\Delta t^2, \Delta\xi^2, \Delta\eta^2\right] \end{aligned} \tag{2.84}$$

Examination of Eq 2.75 reveals

$$\begin{aligned} U_{tt} \;=\; & \left(\hat{B}^2 + \hat{B}_1^2 - \hat{B}\hat{B}_1 - \hat{B}_1\hat{B}\right) U_{\eta\eta} \\ & + \left(\hat{A}_1\hat{B}_1 + \hat{B}_1\hat{A}_1 - \hat{A}_1\hat{B} - \hat{B}\hat{A}_1 - \hat{A}\hat{B}_1 - \hat{B}_1\hat{A} + \hat{A}\hat{B} + \hat{B}\hat{A}\right) U_{\xi\eta} \\ & + \left(\hat{B}_1\hat{B}_2 + \hat{B}_2\hat{B}_1 - \hat{B}\hat{B}_2 - \hat{B}_2\hat{B}\right) U_{\eta\eta\eta} + \hat{B}_2^2 U_{\eta\eta\eta\eta} \\ & + \left(\hat{B}_3\hat{B}_1 + \hat{B}_1\hat{B}_3 - \hat{B}_3\hat{B} - \hat{B}\hat{B}_3 + \hat{B}_1\hat{A}_3 + \hat{A}_3\hat{B}_1\right. \\ & \left. - \hat{B}\hat{A}_3 - \hat{A}_3\hat{B} + \hat{B}_2\hat{A}_1 + \hat{A}_1\hat{B}_2 - \hat{B}_2\hat{A} - \hat{A}\hat{B}_2\right) U_{\xi\eta\eta} \\ & + \left(\hat{B}_2\hat{B}_3 + \hat{B}_3\hat{B}_2 + \hat{B}_2\hat{A}_3 + \hat{A}_3\hat{B}_2\right) U_{\xi\eta\eta\eta} \\ & + \left(\hat{B}_3^2 + \hat{A}_3^2 + \hat{A}_2\hat{B}_2 + \hat{B}_2\hat{A}_2 + \hat{A}_3\hat{B}_3 + \hat{B}_3\hat{A}_3\right) U_{\xi\xi\eta\eta} \end{aligned}$$

$$
\begin{aligned}
&+\left(\hat{A}_3\hat{A}_1+\hat{A}_1\hat{A}_3-\hat{A}_3\hat{A}-\hat{A}\hat{A}_3+\hat{A}_1\hat{B}_3+\hat{B}_3\hat{A}_1\right.\\
&\left.-\hat{A}\hat{B}_3-\hat{B}_3\hat{A}+\hat{A}_2\hat{B}_1+\hat{B}_1\hat{A}_2-\hat{A}_2\hat{B}-\hat{B}\hat{A}_2\right)U_{\xi\xi\eta}\\
&+\left(\hat{A}_2\hat{A}_3+\hat{A}_3\hat{A}_2+\hat{A}_2\hat{B}_3+\hat{B}_3\hat{A}_2\right)U_{\xi\xi\xi\eta}\\
&+\left(\hat{A}^2+\hat{A}_1^2-\hat{A}\hat{A}_1-\hat{A}_1\hat{A}\right)U_{\xi\xi}\\
&+\left(\hat{A}_1\hat{A}_2+\hat{A}_2\hat{A}_1-\hat{A}\hat{A}_2-\hat{A}_2\hat{A}\right)U_{\xi\xi\xi}+\hat{A}_2^2U_{\xi\xi\xi\xi}
\end{aligned}
\tag{2.85}
$$

Since the term of $O[\Delta t]$ in the truncation error of Eq 2.84 does not vanish upon substitution of Eq 2.85, the scheme obtained by adding central-difference representations of the viscous terms to the Euler scheme, Eqs 2.80 through 2.83, is first-order accurate in time and second-order accurate in space. This new scheme represents

$$
\begin{aligned}
U_t+\xi_xF_\xi+\eta_xF_\eta+\xi_yG_\xi+\eta_yG_\eta &= \xi_xF_{v_\xi}+\eta_xF_{v_\eta}+\xi_yG_{v_\xi}+\eta_yG_{v_\eta}\\
&\quad +O\left[\Delta t,\Delta\xi^2,\Delta\eta^2\right]
\end{aligned}
\tag{2.86}
$$

This first-order time, second-order space scheme is hereafter referred to as ATNSC1 which is shorthand for 1st-Order AFIT TVD Navier-Stokes Code.

2.5 Baldwin-Lomax Turbulence Model

Since this effort represents a first step in determining the performance of TVD schemes in conjuction with a turbulence model, the Baldwin-Lomax algebraic turbulence model [3] was chosen for simplicity. The effects of turbulence are simulate by adding an eddy viscosity μ_t to the molecular viscosity μ, with the total viscosity thus given by $\mu+\mu_t$. The heat flux terms are calulated by replacing $k/C_p=\mu/Pr$ with $k/C_p=\mu/Pr+\mu_t/Pr_t$. It is a two layer model with the turbulent eddy viscosity given by

$$
\mu_t=\begin{cases}(\mu_t)_{inner} & (y\le y_{crossover})\\ (\mu_t)_{outer} & (y_{crossover}<y)\end{cases}
\tag{2.87}
$$

where y is the distance away from the surface, in the normal direction. The

value of y at which the inner and outer eddy viscosites are first equal is designated as $y_{crossover}$

The Baldwin-Lomax model utilizes the following formulation for the inner region eddy viscosity

$$(\mu_t)_{inner} = \rho l^2 |\omega| \tag{2.88}$$

with the length scale given by

$$l = ky\left[1 - exp\left(-y^+/A^+\right)\right] \tag{2.89}$$

the vorticity calculated as

$$|\omega| = \left|\frac{\partial u}{\partial y} - \frac{\partial v}{\partial x}\right| \tag{2.90}$$

and the boundary layer coordinate y^+ defined as

$$y^+ = \frac{\sqrt{\rho_w \tau_w} y}{\mu_w} \tag{2.91}$$

The outer region eddy viscosity is calculated according to

$$(\mu_t)_{outer} = KC_{cp}\rho F_{wake} F_{Kleb}(y) \tag{2.92}$$

with

$$F_{wake} = \min \begin{cases} y_{max} F_{max} \\ C_{wk} y_{max} u_{dif}^2 / F_{max} \end{cases} \tag{2.93}$$

F_{max} is the maximum of the function

$$F(y) = y|\omega| \left[1 - \exp\left(-y^+/A^+\right)\right] \tag{2.94}$$

and y_{max} is the value of y at the location where $F(y)$ is a maximum. The exponential term of Eq. 2.94 is taken to be zero in a wake. F_{Kleb} is the Klebanoff intermittency factor

$$F_{Kleb}(y) = \left[1 + 5.5\left(C_{Kleb}y/y_{max}\right)^6\right]^{-1} \tag{2.95}$$

The difference between the maximum and minimum velocity in a given profile, at a fixed x location, is termed u_{dif} and is given by

$$u_{dif} = \left(\sqrt{u^2+v^2}\right)_{max} - \left(\sqrt{u^2+v^2}\right)_{min} \tag{2.96}$$

The minimum value of velocity is zero when the profile begins or ends at a wall,and is therefore nonzero only in wakes.

Two different transition criteria are used in the current study. The Baldwin-Lomax criteria is to set the eddy viscosity equal to zero when the following condition is met:

$$(\mu_t) < C_{mutm}\mu_\infty \tag{2.97}$$

The second criteria is termed the *zero shear stress test* and is used based on Boyle's [4] reccomendation. Simply stated, transition is assumed to occur when the shear stress reaches zero at a surface.

The constants used in the Baldwin-Lomax model are [3]

$$
\begin{aligned}
A^{+} &= 26 \\
C_{cp} &= 1.6 \\
C_{Kleb} &= 0.3 \\
C_{wk} &= 0.25 \\
k &= 0.4 \\
K &= 0.0168 \\
Pr_t &= 0.9 \\
C_{mutm} &= 14
\end{aligned}
\tag{2.98}
$$

III. Results and Conclusions

3.1 Boundary Conditions for the Inviscid Studies

Appropriate boundary conditions, in conjunction with initial conditions and flow parameters such as Mach number, are necessary to arrive at the particular solution of interest. The boundary conditions are now described in detail.

3.1.1 Inlet and Exit Boundary Conditions. If the inlet velocity is supersonic, all characteristics originate upstream of the computational boundary so the four necessary flow quantities may be specified. Likewise, if the outflow velocity is supersonic all characteristics originate inside the computational domain and the four necessary exit quantities must be extrapolated from the interior. Second-order accurate extrapolation is utilized in the schemes under consideration.

Subsonic inflow and/or outflow presents a more complicated situation. In applying the boundary conditions at the inlet and exit of the domain, it is assumed that these boundaries are sufficiently distant from the cascade so that planar wave disturbances propagate collinearly with the stream function. The disturbances are required to leave the computational domain without reflection, except for the reflection of pressure disturbances at the exit. For subsonic inlet velocities, the inlet boundary conditions are arrived at by first assuming that the inlet is part of an imaginary duct extending infinitely far upstream of the cascade. All waves radiating from the computational domain should pass the inlet, without reflection, and continue travelling upstream for all time. Specification of a constant thermodynamic state at upstream infinity requires the expansion disturbance travelling upstream to behave as a simple wave. This behavior allows the application of one-dimensional characteristic theory at the inlet [17].

For subsonic inflow, only one characteristic runs from the interior of the domain towards the computational boundary. Therefore, three quantities must be specified

while one may be extrapolated from the domain interior. Far upstream, the total pressure, p_{t_∞}, and total temperature, T_{t_∞}, are specified, while only the inlet flow angle, β_2, is specified at the computational boundary. The speed of sound at the inlet, c_2, is extrapolated from the domain interior. The Riemann invariant along the characteristic spanning the expansion wave from leading to trailing edge is given by

$$V_\infty + \frac{2}{\gamma - 1} c_\infty = V_2 + \frac{2}{\gamma - 1} c_2 \tag{3.1}$$

where V is the magnitude of the velocity vector. As the velocity vanishes far upstream, the inlet velocity is obtained from

$$V_2 = \frac{2}{\gamma - 1} (c_\infty - c_2) \tag{3.2}$$

which, along with the inlet flow angle, determines u and v. The inlet pressure is determined from the isentropic relation

$$p_2 = p_\infty \left(\frac{c_2}{c_\infty} \right)^{2\gamma/(\gamma-1)} \tag{3.3}$$

The speed of sound and pressure fix the state point, uniquely determining the density and internal energy.

For subsonic axial Mach numbers, simple-wave theory is also applied at the exit. The exit is treated as an open-end duct that exhausts into a plenum, requiring the exit pressure to match the plenum pressure. Thus, all pressure disturbances are reflected back into the computational domain from the exit. Two characteristics extend from the interior of the computational domain to the exit, while one originates outside the domain. Thus only one quantity, in this case pressure, can be specified at the exit. All other quantities must be extrapolated from the interior of the domain. The quantities chosen for extrapolation are entropy, tangential velocity, and the

Riemann invariant, R_{inv}. The density is obtained from the isentropic relation

$$\rho_3 = (p_3/s_{int})^{1/\gamma} \tag{3.4}$$

where s_{int} is the entropy extrapolated from the interior. The pressure and density fix the state point, uniquely determining the speed of sound and internal energy. With the tangential velocity extrapolated from the interior, the axial velocity is obtained by applying the Riemann invariant in the axial direction:

$$u_3 = R_{inv} - \frac{2}{\gamma - 1} c_3 \tag{3.5}$$

where

$$R_{inv} = u_{int} + \frac{2}{\gamma - 1} c_{int} \tag{3.6}$$

and u_{int} and c_{int} are the axial velocity and speed of sound at the point inside the domain where the Riemann invariant is evaluated.

3.1.2 Periodicity and Blade Boundary Conditions. Only one blade passage of an infinite cascade is analyzed. Therefore, periodicity conditions are applied at cell centers, or ghost points, located outside the computational domain. These points are located along the outer boundary and also along the wake cut when a C-type grid is utilized. For an H-type grid, ghost points are located along the upper and lower boundaries upstream and downstream of the blade. At the blade surface, the only condition that can be specified is the requirement for surface tangency. Since the blade surface is mapped to a constant η coordinate, the normal component of velocity is given by

$$V_n = \frac{\eta_x u + \eta_y v}{\sqrt{\eta_x^2 + \eta_y^2}} \tag{3.7}$$

while the tangential component is

$$V_t = \frac{\eta_y u - \eta_x v}{\sqrt{\eta_x^2 + \eta_y^2}} \tag{3.8}$$

The requirement for surface tangency is met by setting

$$V_{t_{j,0}} = V_{t_{j,1}} \tag{3.9}$$

and

$$V_{n_{j,0}} = -V_{n_{j,1}} \tag{3.10}$$

where j is the ξ index, 0 represents a ghost point just inside the body, and 1 is the index of the first cell center above the body. Cell centers and ghost points are used to place the blade surface along the interface of the grid cell and ghost cell. This mesh system helps ensure both consistent and conservative boundary conditions [34]. The inverse relation between the Cartesian velocities and Eqs 3.8 and 3.7 then gives

$$\begin{bmatrix} u_{j,0} \\ v_{j,0} \end{bmatrix} = \frac{1}{\sqrt{\eta_x^2 + \eta_y^2}} \begin{bmatrix} \eta_y & \eta_x \\ -\eta_x & \eta_y \end{bmatrix} \begin{bmatrix} V_{t_{j,0}} \\ V_{n_{j,0}} \end{bmatrix} \tag{3.11}$$

The pressure at the ghost points is obtained by applying the normal-momentum equation at the first line of cell centers above the body [32]:

$$\begin{aligned} -\rho \left(\xi_x u + \xi_y v\right)\left(\eta_x u_\xi + \eta_y v_\xi\right) &= \left(\eta_x \xi_x + \xi_y \eta_y\right) p_\xi + \left(\eta_x^2 + \eta_y^2\right) p_\eta \\ &= p_n \sqrt{\eta_x^2 + \eta_y^2} \end{aligned} \tag{3.12}$$

Central differences are used for both the ξ and η derivatives.

One additional property is needed to fix the state of the ghost points. In the present study, an adiabatic wall condition is chosen to provide this final property:

$$T_n = 0 \tag{3.13}$$

Although it is inconsistent with the Euler equations to specify either the temperature or its gradient at the blade surface [34], an adiabatic wall condition has been used by others [32] and yields results that agree well with theory and experiment.

3.2 Boundary Conditions for Viscous Flow

Boundary conditions for viscous flows are, in general, more straight forward than their inviscid counterparts described in Section 3.1. At the wall, the inviscid surface tangency condition, Eqs 3.7 and 3.8, is replace by the viscous no-slip requirement:

$$\begin{aligned} u &= 0 \\ v &= 0 \end{aligned} \tag{3.14}$$

Simplified wall temperature contitions representing either an adiabatic wall

$$T_{w_n} = 0 \tag{3.15}$$

or constant temperature wall

$$T_w = C \tag{3.16}$$

are used in the current study, depending on the flow of interest. With the wall mapped to a constant η coordinate, the pressure at the wall is obtained by solving

the normal-momentum equation:

$$
\begin{aligned}
p_n\sqrt{\eta_x^2+\eta_y^2} &= (\xi_x\eta_x+\xi_y\eta_y)\,p_\xi+\left(\eta_x^2+\eta_y^2\right)p_\eta \\
&= (\xi_y v_\xi+\eta_y v_\eta)\left\{\eta_x\left(\xi_x\lambda_\xi+\eta_x\lambda_\eta\right)\right. \\
&\quad \left.+\eta_y\left[\xi_y\left(2\mu+\lambda\right)_\xi+\eta_y\left(2\mu+\lambda\right)_\eta\right]\right\} \\
&\quad +(\xi_y u_\xi+\eta_y u_\eta)\left\{\eta_x\left(\xi_y\mu_\xi+\eta_y\mu_\eta\right)+\eta_y\left(\xi_x\mu_\xi+\eta_x\mu_\eta\right)\right\} \\
&\quad +\mu\eta_x\left(\xi_y^2 u_{\xi\xi}+2\xi_y\eta_y u_{\xi\eta}+\eta_y^2 u_{\eta\eta}\right) \\
&\quad +(2\mu+\lambda)\eta_y\left(\xi_y^2 v_{\xi\xi}+2\xi_y\eta_y v_{\xi\eta}+\eta_y^2 v_{\eta\eta}\right)
\end{aligned}
\tag{3.17}
$$

Flow at the inlet and exit of the computational domain is assumed to be inviscid. Inflow and outflow relations from Section 3.1 are thus used to determine flow quantities at these boundaries. As stated in Section 3.1, for supersonic outflow all quantities must be extrapolated from the interior of the domain. In practice, this extrapolation is also performed in the subsonic boundary-layer embedded in the supersonic outflow. For the cases to be considered herein, no adverse effects of this extrapolation are noted.

3.3 Shock-Boundary Layer Interaction

An indepth experiment in laminar shock-boundary-layer interaction was carried out by Hakkinen et al. [19] in 1959 at the Massachusetts Institute of Technology under the sponsorship of the National Advisory Committee for Aeronautics. Detailed measurements were made of pressure distribution, skin friction coefficient, and velocity profiles for a number of combinations of overall pressure ratio, p_f/p_∞, and shock Reynolds number, Re_{x_s}, at a freestream Mach number of 2.0 for a shock wave impinging upon a flat plate boundary-layer.

The experimental pressure and skin friction profiles for this case are shown in Fiqure 3.1, and a sketch of the wave structure is shown in Figure 3.2. The friction

coefficient, C_f, is defined as

$$C_f \equiv \frac{\tau_w}{q_\infty} \tag{3.18}$$

where τ_w is the normal component of shear stress at the wall

$$\tau_w \equiv \mu V_{t_n} \tag{3.19}$$

and q_∞ is the dynamic pressure

$$q_\infty = \frac{1}{2}\rho_\infty V_\infty^2 \tag{3.20}$$

With the tangential velocity given by Eq 3.8, and the wall mapped to a η = constant coordinate, τ_w can be written as

$$\tau_w = \mu\left(\eta_y u_\eta - \eta_x v_\eta\right) \tag{3.21}$$

No negative values of skin friction are shown because the total-head tube was not able to reliably indicate negative shear values.

A typical grid used for the numerical investigations is shown in Figure 3.3. Spacing is held constant in the axial direction at $\Delta x/x_{shock} = 0.013$ and the minimum spacing in the normal direction is dicated by specifing $y^+_{ref} = 2.2$ per Boyle [4]. The computational domain is initialized at the uniform freestream conditions to the left of the point along the upper boundary at which the shock is generated. Post-shock conditions are applied downstream of this point. An adiabatic wall condition is used to obtain the wall temperature along the plate and the nomal momentum equation is solved to obtain the wall pressure in combination with the no-slip velocity constraint at the wall.

Figure 3.4 depicts the solution obtained with $\epsilon = 0$ in the nonlinear fields and $\epsilon = 0.025$ in the linearly degenerate fields, based on the author's previous work /citedr:91. The pressure profile of Figure 3.4 clearly shows the pressure rise to separation,

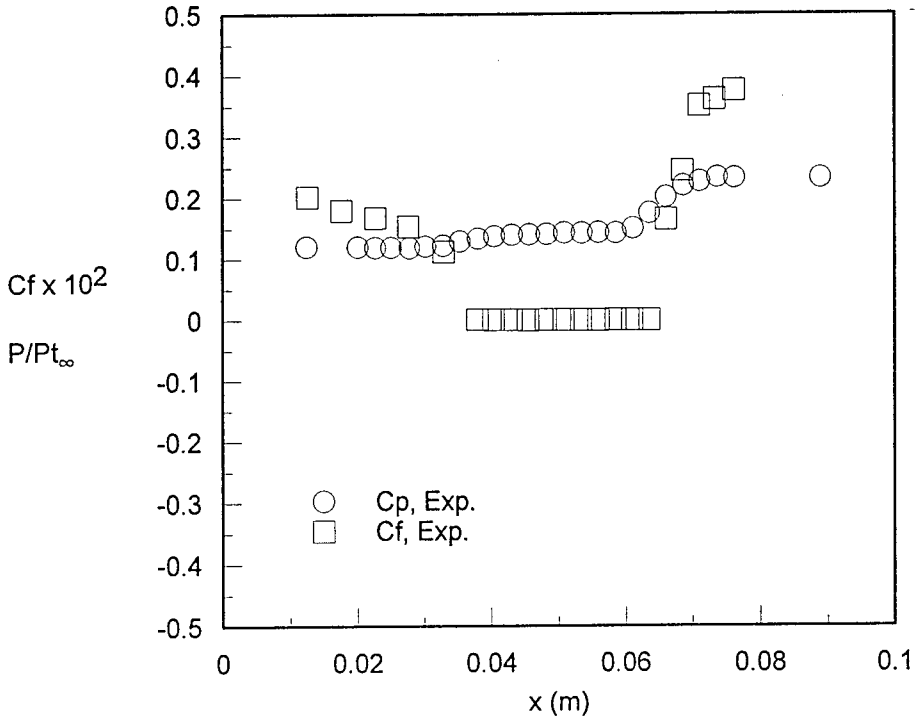

Figure 3.1. Experimental Pressure and Skin Friction Profiles

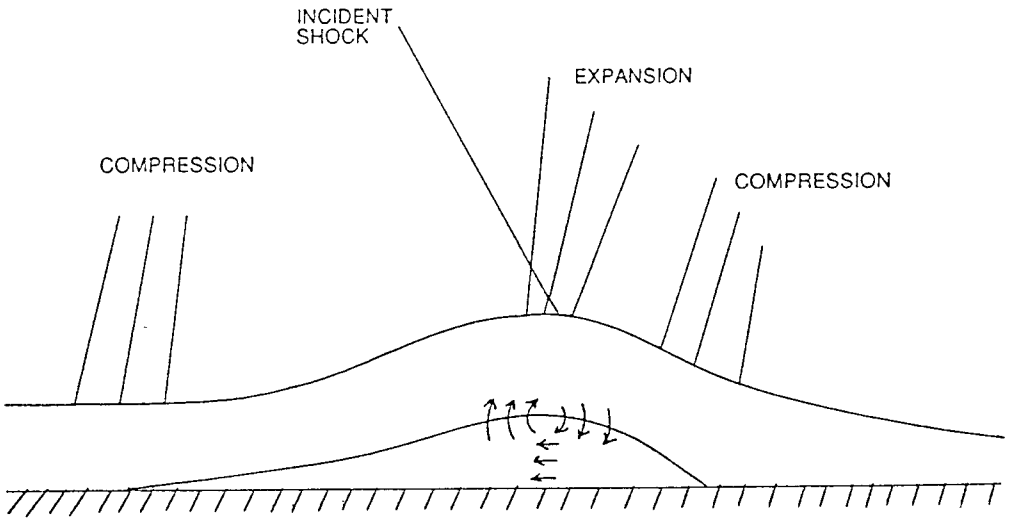

Figure 3.2. Flowfield Structure

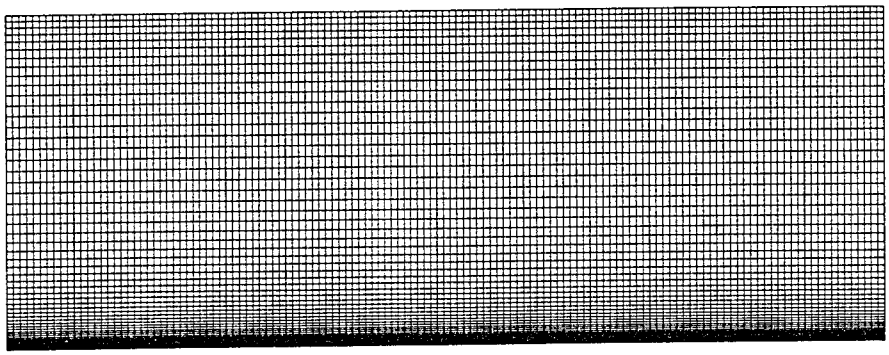

Figure 3.3. Grid Used in Shock-Boundary Layer Interaction Investigations

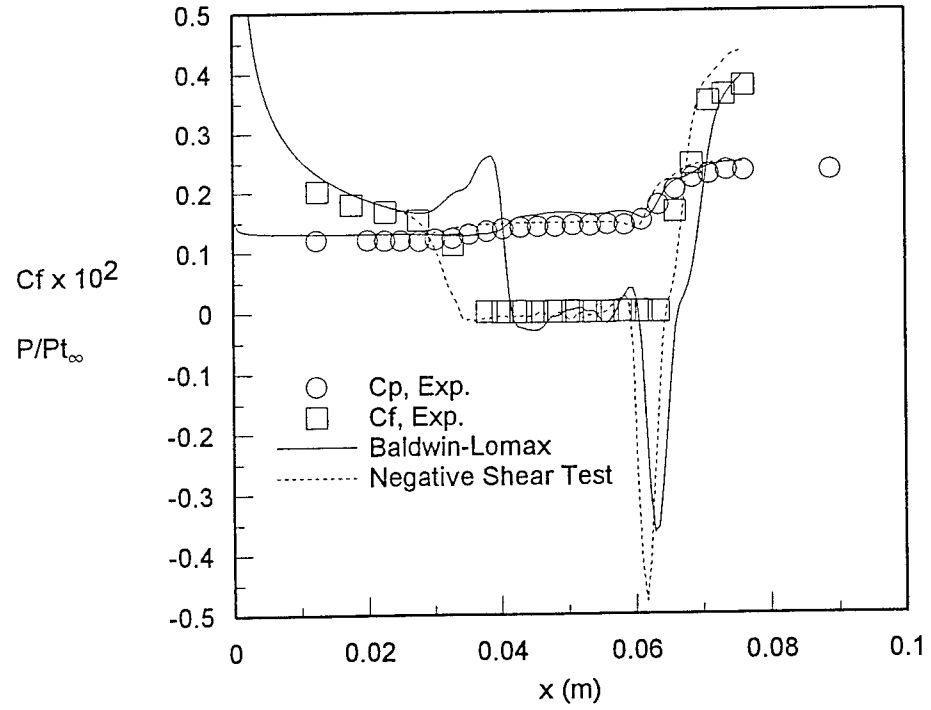

Figure 3.4. Pressure and Skin Friction Profiles

the constant pressure plateau within the separated region, and the pressure rise to reattachment as described in reference [19]. The most noticeable aspect of the pressure profile is the erratic behavior in the separated region when the Baldwin-Lomax transition criteria is used. Use of the negative shear test to determine the transition location results in a much smoother pressure profile in the separated region. The skin friction profile of Figure 3.4 contains several regions of interest. Using the Baldwin-Lomax separation criteria, there is an increase in the friction coefficient leading up to the sharp drop just prior to separation. The Baldwin-Lomax transition criteria resulted in delayed separation while the negative shear test criteria led to a closer match with the experimental data. The skin friction profile beyond reattachment shows a rapid rise to the ultimate value for both transition criteria.

The solutions obained using the ATNSC TVD algorithm clearly demonstrate that it is possible to obtain very accurate estimations of separation and reattachment points as well as pressure and skin friction profiles. ATNSC solutions are obtained using a constant CFL number of 0.95, under the time step restriction of Eq 1.28. The solution is monitored until no change is observed in the skin friction profile, typically requiring 100000 time steps to achieve steady-state convergence with $y^+_{ref} = 2.2$.

3.4 High-Work Low-Aspect-Ratio Turbine

The ATNSC scheme is next applied to a rotor cascade whose heat transfer characteristics were studied experimentally by Hippensteele, Russell and Torres [25] and computationally by Boyle [4]. The comparisons shown herein are based upon the design Reynold's number of 7.6×10^5 based on the blade chord.

Figure 3.5 is a typical C-type grid used for this analysis. The actual grid used is made up of 285×46 points. Points are clustered at the leading and trailing edges for improved resolution. 25 points are placed along the portion of the C-type grid representing the inlet.

Consistent with subsonic inflow at the computational inlet, the total pressure

and total temperature in the quiescent region infinitely far upstream of the cascade are required as boundary conditions. The values used are $p_{t_\infty} = 11.87 \times 10^4 N/m^2$ and $T_{t_\infty} = 303.00K$. The static pressure at station 3, the rotor exit, is input as the exit pressure. In particular, $p_3 = 8.47 \times 10^4 N/m^2$. For the viscous calculations, the surface temperature is held constant at $T_w = 333.33K$ consistent with Boyle's work [4, 5]. The initial conditions applied for the present study are referred to as "cascade tunnel start" conditions because of the analogy to the starting of a blow-down cascade tunnel. The domain is initialized at zero velocity, the pressure and temperature corresponding to that in the quiescent region upstream of the inlet. This is analogous to placing a diaphragm at the exit of the computational domain. At time t_0, the solution is started and a centered expansion wave propagates upstream. It is also possible to place the diaphragm anywhere in the computational domain, but placing it at the exit avoids the formation of a contact surface that must pass through the domain. While the present TVD scheme has demonstrated the ability to resolve such a contact surface in very fine detail, convergence is slowed due to the fact that the contact surface progresses through the domain at the convective velocity.

When the cascade tunnel start is used and the diaphragm is placed at the exit of the computational domain, a centered expansion wave propagates upsteam through the blade passage and towards the inlet. As the leading edge of the expansion wave reaches the leading edge of the airfoil, circulation is established around the blade through the shedding of a starting vortex from the airfoil. The vortex is convected downstream and eventually exits the computational domain without being reflected.

Figures 3.6 and 3.7 represent the solution obtained when the TVD methodology is applied to this case. Figure 3.6 compares the surface pressures obtained from the Euler TVD solution with Boyle's Euler solution [4]. The TVD solution shows better agreement with the data except in the area of the trailing edge. This is explained by the fact that Boyle's calculations were performed on blade with a cusp added

to the trailing edge. The current solution was computed for a blunt trailing edge, since addinga cusp forces the location of the stagnation point to occur at the sharp trailing edge. This in turn specifies the circulation around the blade.

Figure 3.7 compares the Stanton numbers obtained in the present effort with those computed by Boyle [4]. Boyle's turbulence model incorporated the effects of pressure gradient and freestream turbulence into the standard Baldwin-Lomax model. The present effort utilizes the standard Baldwin-Lomax model only. The ATNSC solution follows the general trend of the experimental data, except in the region just downstream of the transition location on the pressure surface. Boyle reports that his calculations predicted early transition on the suction surface. It appears that his calculations actually predict suction and pressure surface transtion much too late. The ATNSC calculations, as well as the experimental data [25], show that the large increase in heat transfer near the suction surface trailing edge is actually due to flow separation, not transition. This is shown graphically in Figure 3.8. Transition occurs near the leading edge on both the suction and pressure surfaces.

The steady-state solution obtained with the TVD formulation compares extremely well against the experimental data. This level of agreement provides an excellent argument for the use of TVD schemes in computing transonic cascade flows.

CFL numbers as high as 0.95 were consistently used to obtain steady-state results. In fact, the CFL number was dropped to 0.5 only if a contact surface was in the vicinity of the rounded trailing edge of the blade. At all other times the CFL number was maintained at 0.95. This is in contrast to CFL numbers as low as 0.2 required during startup and only as high as 0.8 to maintain stability when using the MacCormack scheme [15, 17]. A typical, time-accurate calculation requires approximately 100,000 operator sweeps to achieve steady state convergence for the turbulent computations.

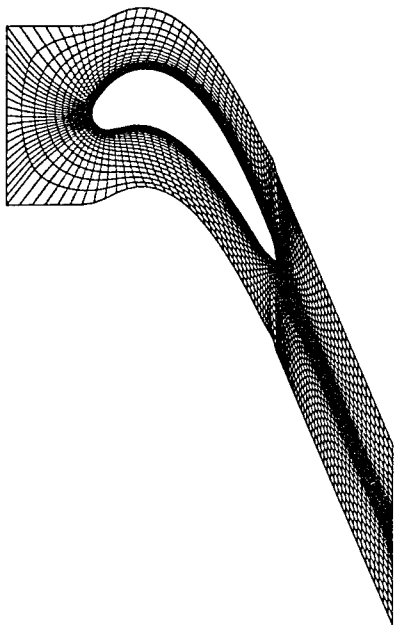

Figure 3.5. Typical C-type Grid Used in the Present Analysis

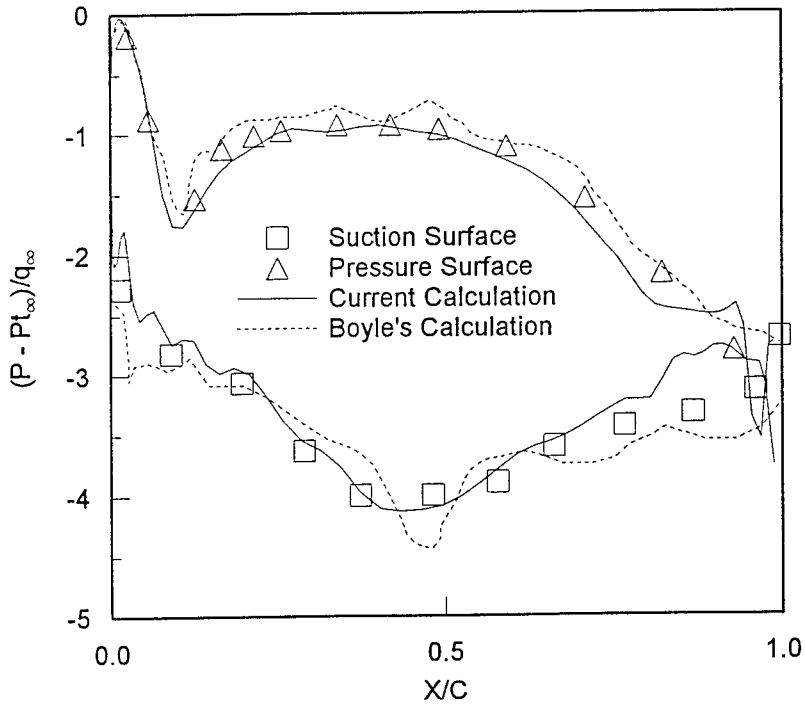

Figure 3.6. Surface Pressures

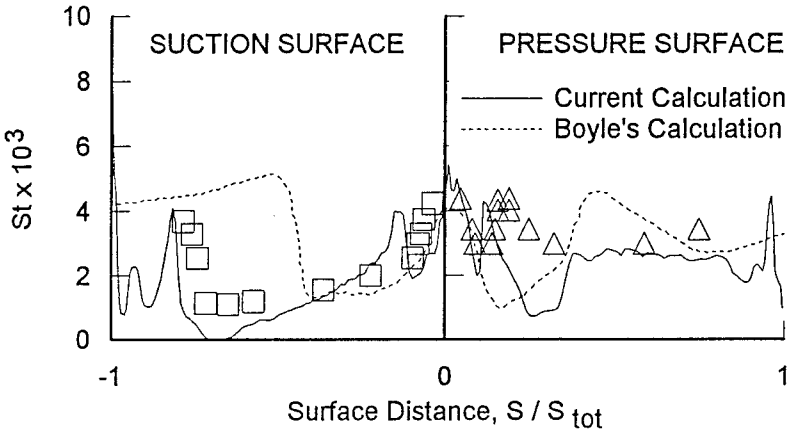

Figure 3.7. Stanton Number

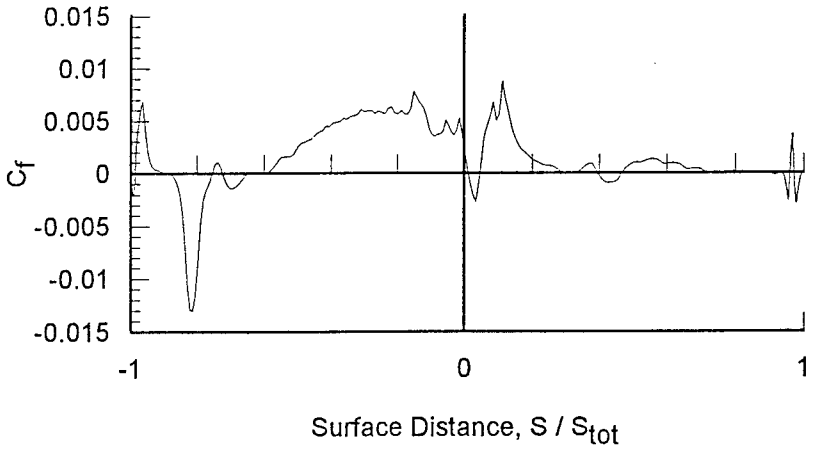

Figure 3.8. Friction Coefficient

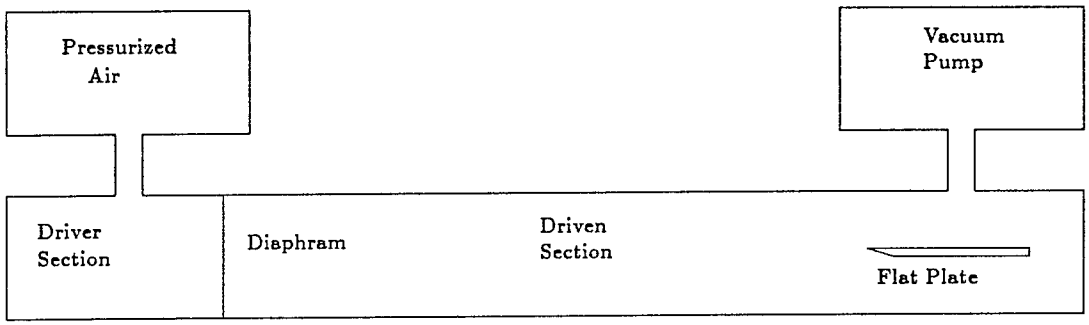

Figure 3.9. Flat Plate Mounted in Shock Tube

3.5 Unsteady Shock-Induced Heat Transfer

The final test case for the ATNSC algorithm is the prediction of unsteady heat transfer due to a shock wave moving down a flat plate. The origin of this test case is the work of Smith [39] who used a shock tube to study the heat transfer to a sharp-edged flat plate, creating ratios of gas temperature to surface temperature typical of those in gas turbine engines. A schematic of Smith's experimental appartus is shown in Figure 3.9.

The case under consideration here is representative of data set A of Smith [39]. The governing parameters are the shock Mach number (M_s), pressure in the driven section (P_1), and temperature in the driven section (T_1). The wall temperature on the flat plate is held constant in the calculations at T_1. Using $M_s = 1.095$, $P_1 = 49102.800\ N/m^2$, and $T_1 = 297.428\ K$ results in a shock pressure ratio of 1.232, a temperature ratio of 1.062, a steady velocity behind the shock of 52.368 m/s, a steady Mach number behind the shock of 0.147, and a steady Reynolds number behind the shock of 92482. Shock Mach number, driven section pressure, and driven section temperature are consistent with data set A of reference [39]. Experimental measurements of the shock Mach number are only accurate within $\pm 2\%$ and can significantly effect the level of agreement [39] between theory, experiment, and numerical solution. Thus, the numerical solutions used the nominal shock Mach

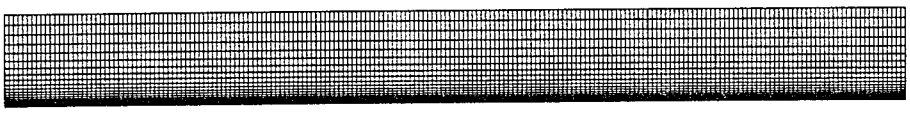

Figure 3.10. Grid for Heat Flux Solutions

number of 1.095 for comparison. A solution for $M_s = 1.117$, 2% above nominal, is also presented.

Initial conditions for the computations consist of placing the shock just ahead of the plate at time zero by establishing pre-shock and post-shock conditions on either side of the point selected. The shock is then allowed to move freely as time progresses. With the temperature held at T_1 the normal momentum equation is solved to obtain the pressure at the wall, in combination with the no-slip constraint at the wall. The numerical solution is sampled at a point $5.080 \times 10^{-2} m$ downstream of the leading edge to obtain the heat flux at this point. This point was chosen consistent with the first sampling point of Smith in the shock tube experiment. The computations are carried out to a time of approximately one millisecond, the approximate time of transition to turbulent flow as noted by Smith [39]. A typical grid used in this study is shown in Figure 3.10. This grid consists of 201 points in the axial direction and 31 points in the normal direction. The grid spacing is held constant in the axial direction at $\Delta x = 2.540 \times 10^{-3} m$ with the initial spacing from the wall consistent with $y^+_{ref} = 2.2$.

Figure 3.11 is the solution obtained with ϵ values of $\epsilon_1 = \epsilon_2 = \epsilon_3 = \epsilon_4 = 0.0$, based upon the numerical experiments of the author [16]. Time is referenced to the time of the shock wave passing the sampling point. The peak heat flux agrees well with experiment for both shock Mach numbers. The Baldwin-Lomax transition criteria failed to initiate transition for either case. Because the transition mechanism

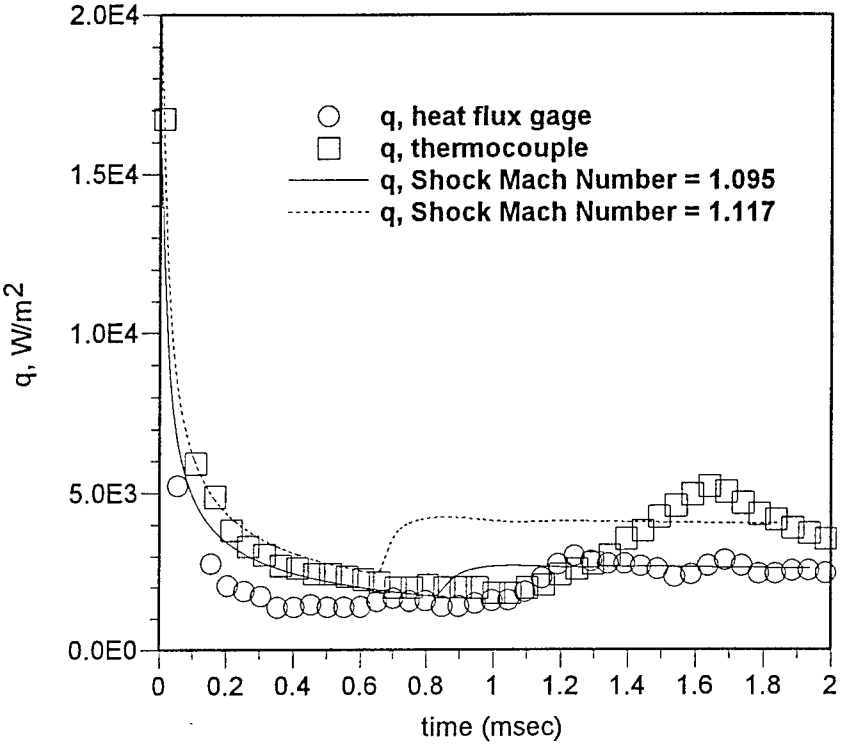

Figure 3.11. Heat Flux History

is not well understood for this experiment [39], the boundary layer was artificially forced to transition at the leading edge in the computations. At the higher shock Mach number this results in a very early transition, but the final heat flux level is in good agreement with the thermocouple data after approximately 1.8 msec. At the lower shock Mach number, transition again occurs early but the final heat flux level agrees well with the heat flux gage data. It is clear from these results that much more effort is needed in an attempt to understand the transition mechanism for this situation. All ATNSC solutions are undertaken at a CFL of 0.95, with the time step restriction of Eq 1.28. This results in approximately 25,000 sweeps to arrive at a time of 2.0 msec.

3.6 Conclusions

TVD methodolgy has been applied to problems not previously examined using TVD schemes. Early TVD research concentrated mainly on supersonic and hyper-

sonic flows, both inviscid and viscous, and was almost solely directed toward obtaining steady-state solutions. Later effort by the author [16] extended the TVD methodology to inviscid transonic cascade flows, viscous flows with shock-induced laminar boundary-layer separation, and unsteady laminar flows with signifcant shock-induced heat transfer. The current effort has extended the TVD methodology to both steady and unsteady turbulent flows.

Shock-boundary-layer interaction has been studied by numerous researchers using highly regarded algorithms such as the MacCormack [29], Dawes [10], Beam-Warming [11], and Newton [28] methods. While acceptable predictions of the pressure profile in the boundary-layer have often been computed, TVD schemes have enabled researchers to accurately compute the skin friction profile [16]. The ATNSC algorithms finally provide the means to accurately compute pressure profiles, separation and reattachment locations, and skin friction profiles in good agreement with the available experimental data. Results given in Section 3.3 are testament to this.

Cascade flows are currently of great interest to gas turbine engine designers and researchers [2, 14, 13]. Analysis of these flows is a severe test of an algorithm because of the wide Mach number range, typically $0.3 \leq M \leq 1.3$, and the fact that the flow is confined in a passage where wave systems tend to reflect back into the domain. Results presented in Section 3.4 show that the TVD schemes of Sections 2.2.1 and 2.2.2 yield steady-state results in good agreement with experiment, compared to other methods.

Unsteady shock-induced heat transfer has been studied theoretically [30, 31], experimentally [14, 39], and has recently become of interest computationally [16]. The increased interest is due to the enhanced system performance available through accurate knowlege of the heat transfer [6]. However, it is not uncommon for computed heat flux values to be an order-of-magnitude different from experimental values [18]. The ATNSC algorithms represent a significant advancement in the state-of-the-art for computing shock-induced heat transfer.

3.7 Further Research

Performance of the ATNSC algorithms with enhanced turbulence models, accounting for freestream turbulence, pressure gradient, etc., should be investigated. These enhancements were not possible in this limited first evaluation of TVD performance with turbulence modeling included. The current investigation shows that implementation of the simple Baldwin-Lomax algebraic turbulence model correctly predicts both skin friction and heat flux in the turbulent region.

Overall, the TVD based viscous algorithms perform exceptionally well on the test cases herein. Emphasis must be placed on applying these algorithms to even more rigorous test cases so as to gain an even greater understanding of their weaknesses as well as their strengths.

Bibliography

1. Anderson, Dale A., John C. Tannehill, and Richard H. Pletcher. *Computational Fluid Mechanics and Heat Transfer.* Series in Computational Methods in Mechanics and Thermal Sciences. New York: Hemisphere Publishing Corporation, 1984.

2. Air Force Wright Aeronautical Laboratory. *IHPTET, Integrated High Performance Turbine Engine Technology Initiative.*AFWAL/POT Brochure.

3. Baldwin, B. S. and H. Lomax. "Thin Layer Approximation and Algebraic Model for Separated Turbulent Flows," *AIAA 16th Aerospace Sciences Meeting.* AIAA-78-257. (January 1978).

4. Boyle, R. J. "Navier-Stokes Analysis of Turbine Blade Heat Transfer." *Gas Turbine and Aeroengine Conference.* ASME Paper No. 90-GT-42. (June 1990).

5. Boyle, R. J. National Aeronautics and Space Administration, Lewis Research Center. Private communications. (1994).

6. Brahney, James H. "Propulsion Systems for the '90s." *Aerospace Engineering,* August 1990.

7. Chakravarthy, S.R. ,K-Y Szema, U.C. Goldberg, J.J. Gorski , and S. Osher. "Application of a New Class of High Accuracy TVD Schemes to the Navier-Stokes Equations,"*AIAA 23rd Aerospace Sciences Meeting.* AIAA-85-0165. (January 1985).

8. Chapman, D. R., D. M. Kuehn and H. K. Larson.*Investigation of Separated Flows in Supersonic and Subsonic Streams with Emphasis on the Effect of Transition.* NACA Technical Report 1356 (1958).

9. Courant, R. and K. O. Friedrichs. *Supersonic Flow and Shock Waves.* Applied Mathematical Sciences, Volume 21. New York: Springer-Verlag, 1976.

10. Dawes, W.N. " Efficient Implicit Algorithm for the equations of 2-D Viscous Compressible Flow: Application to Shock- Boundary Layer Interaction," *Journal of Heat & Fluid Flow*, Volume 4, Number 1:17-26 (March 1983).

11. Degrez, G., C.H. Boccadoro and J.F. Wendt. "The Interaction of an Oblique Shock Wave with a Laminar Boundary Layer Revisited. An Experimental and Numerical Study," *Journal of Fluid Mechanics*, Volume 177:247-263 (1987).

12. Denton, J. D. "An Improved Time Marching Method for Turbomachinery Flow Calculation." ASME Paper No. 82-GT-239, *Journal of Engineering for Power*, Vol. 105, July 1983.

13. Dix, Donald M. and James S. Petty. "Aircraft Engine Technology gets a second wind," *Aerospace America,* July 1990.

14. Doorly, D. J. and M. L. G. Oldfield. " Simulation of Shock Wave Passing on a Turbine Rotor," *Journal of Engineering for Gas Turbines and Power,*Volume 107: 998-1006 (October 1985).

15. Driver, Mark A. *Development of a Shock Capturing Code for Use as a Tool in Designing High-Work Low Aspect Ratio Turbines.* MS Thesis, AFIT/GAE/AA/88D-10. School of Engineering, Air Force Institute of Technology (AU), Wright-Patterson AFB OH, December 1988 (AD-A202 706).

16. Driver, Mark A. *High-Resolution TVD Schemes for the Analysis of I. Inviscid Supersonic and Transonic Flows II. Viscous Flows with Shock- Induced Separation and Heat Transfer.* Ph.D. Dissertation, AFIT/DS/AA/91-2. School of Engineering, Air Force Institute of Technology (AU), Wright-Patterson AFB OH, December 1991).

17. Driver, Mark A., and Robert E. Gray. "Application of Simple Wave Theory to the Radiative Boundary Conditions Required for an Internal Flow Euler Solver," *AIAA/ASME/SAE/ASEE 25th Joint Propulsion Conference.* AIAA-89-2577. (July 1989).

18. Gray, Robert. Air Force Aero-Propulsion and Power Laboratory. Private communications. (1990).

19. Hakkinen, R. J., I. Greber, L. Trilling and S. S. Abarbanel. *The Interaction of an Oblique Shock Wave with a Laminar Boundary Layer.* NASA Memorandum 2-18-59W. Washington DC: (March 1959).

20. Harten, Amiram. *The Method of Artificial Compression: I. Shocks and Contact Discontinuities.* AEC Research & Development Report COO-3077-50, Courant Institute, New York University. June 1974

21. Harten, Amiram. "The Artificial Compression Method for Computation of Shocks and Contact Discontinuities. I. Single Conservation Laws," *Communications on Pure and Applied Mathematics.* Volume XXX: 611-638 (1977).

22. Harten, Amiram. "The Artificial Compression Method for Computation of Shocks and Contact Discontinuities. III. Self- Ajusting Hybrid Schemes," *Mathematics of Computation.* Volume 32: 363-389 (1978).

23. Harten, Ami. "High Resolution Schemes for Hyperbolic Conservation Laws," *Journal of Computational Physics.* Volume 49: 357-393 (1983).

24. Harten, A., J.M. Hyman and P.D. Lax. "On Finite- Difference Approximations and Entropy Conditions for Shocks," *Communications on Pure and Applied Mathematics.* Volume XXIX: 297-322 (1976).

25. Hippenstelle, S.A., L.M. Russell and F.J. Torres. "Local Heat-Transfer Measurements on a Large Scale-Model Turbine Blade Airfoil Using a Composite of a Heater Element and Liquid Crystals," *Journal of Engineering for Gas Turbines and Power.* Volume 107: 953-960 (1985).

26. Josyula, Eswar, Datta Gaitonde and Joseph Shang. "Nonequilibrium Hypersonic Flow Solutions Using the Roe Flux- Difference Split Scheme," *AIAA 22nd Fluid Dynamics, Plama Dynamics & Lasers Conference.* AIAA-91-1700. (June 1991).

27. Lin, Herng and Ching-Chang Chieng. "Comparisons of TVD Schemes for Turbulent Transonic Projectile Aerodynamics Computations," *AIAA 29th Aerospace Sciences Meeting.* AIAA-91-0171. (January 1991).

28. Liou, Meng-Seng. " A Newton/Upwind Method and Numerical Study of Shock Wave/Boundary Layer Interactions," *International Journal for Numerical Methods in Fluids*, Volume 9:747-761 (1989).

29. MacCormack, Robert W. "Numerical Solution of the Interaction of a Shock Wave With a Laminar Boundary Layer," *Lecture Notes in Physics*,Volume 8:151-163 (1971).

30. Mirels, Harold. *Laminar Boundary Layer Behind Shock Advancing into Stationary Fluid.* NACA Technical Note 3401. Cleveland Ohio: Lewis Flight Propulsion Laboratory, March 1955.

31. Mirels, Harold. *Laminar Boundary Layer Behind Shock or Thin Expansion Wave Moving into Stationary Fluid.* NACA Technical Note 3712. Cleveland Ohio: Lewis Flight Propulsion Laboratory, May 1956.

32. Pulliam, Thomas H. and Joseph L. Steger. "Recent Improvements in Efficiency, Accuracy, and Convergence for Implicit Approximate Factorization Algorithms," *AIAA 23rd Aerospace Sciences Meeting.* AIAA-85-0360. (January 1985).

33. Riedelbauch, S. and G. Brenner. " Numerical Simulation of Laminar Hypersonic Flow Past Blunt Bodies Including High Temperature Effects," *AIAA 21st Fluid Dynamics, Plasma Dynamics and Lasers Conference.* AIAA-90-1492. (June 1990).

34. Roache, Patrick J. *Computational Fluid Dynamics.* Albuquerque: Hermosa Publishers, 1972.

35. Roe, P. L. "Approximate Riemann Solvers, Parameter Vectors, and Difference Schemes," *Journal of Computational Physics*, Volume 43: 357-372 (1981).

36. Schlichting, Hermann. *Boundary-Layer Theory*(Seventh Edition). New York: McGraw-Hill Book Company, 1979.

37. Scott, J. N. and W. L. Hankey, Jr. "Boundary Conditions for Navier-Stokes Solutions of Unsteady Flow in a Compressor Rotor," *Three Dimensional Flow Phenomena in Fluid Machinery.* 141-151. New York: Fluid Engineering Division of the ASME, November 1985.

38. Shang, J. S. " Numerical Simulation of Wing-Fuselage Aerodynamic Interaction,"*AIAA Journal*,Volume 22, Number 10: 1345-1353 (October 1984).

39. Smith, B.J. *Investigation of Heat Transfer to a Sharp Edged Flat Plate Using a Shock Tube.* MS Thesis, AFIT/GAE/AA/86D-16. School of Engineering, Air Force Institute of Technology (AU). Wright-Patterson AFB OH, December 1986.

40. Yee, H. C. and A. Harten. " Implicit Total Variation Diminishing (TVD) Schemes for Steady-State Calculations." AIAA-83-1902.

41. Yee, H. C. and P. Kutler. *Application of Second- Order-Accurate Total Variation Diminishing (TVD) Schemes to the Euler Equations in General Geometries.* NASA Technical Memorandum 85845. Moffett Field California: Ames Research Center, August 1983.

42. Yee, H. C. *A Class of High-Resolution Explicit and Implicit Shock-Capturing Methods.* NASA Technical Memorandum 101088. Moffett Field California: Ames Research Center, February 1989.

43. Yee, H. C., R. F. Warming, and A. Harten. "Implicit Total Variation Diminishing (TVD) Schemes for Steady-State Calculations," *Journal of Computational Physics.* Volume 57: 327-360 (1985)

44. Wang, J.C.T. and G.F. Widhopf. "A High-Resolution TVD Finite Volume Scheme for the Euler Equations in Conservation Form," *AIAA 25th Aerospace Sciences Meeting.* AIAA-87-0538. (January 1987).

45. White, Frank M. *Viscous Fluid Flow.* New York: McGraw-Hill, 1974.